4^{th} SEMESTER MCE

INVESTIGATION OF TIRE DYNAMICS INFLUENCE ON ARTICULATED FRAME STEERED VEHICLES STEERING PERFORMANCE

30^{th} of May 2024

AALBORG UNIVERSITET

STUDENTERRAPPORT

Mechatronic Control Engineering, Malthe Goosmann
Department of Energy Technology, Aalborg University

Abstract

Dette speciale er udarbejdet med fokus på dækdynamikkens påvirkning af cylindertrykket i en knækstyret gummiged. Formålet med projektet er at udvikle en dynamisk model der ved hjælp af et minimalt antal parametre kan forskrive dækkets påvirkning af trykket i styre cylinderen. Knækstyrede køretøjer kan opleve svingninger i systemet grundet en stor inerti som er ubehagelig for operatøren og derfor er de uønsket i et sådan system.

Kapitel 1 er en introduktion til problemstillingen hvor motivationen bag projektet og køretøjets styremekanisme bliver beskrevet. Efterfølgende bliver systemet beskrevet med udgangspunkt i det køretøj der er stillet til rådighed. Herefter bliver dækkets struktur fremlagt med fokus på radiale dæk, som bliver anvendt som traktordæk. Det beskrives hvordan dækkets ydeevne bliver påvirket af diverse faktorer og hvordan dynamikkerne i et dæk påvirkes af kræfterne fra køretøjet.

I kapitel 2 bliver en ikke-lineær dynamisk model, der modellere dækdynamikken for køretøjet udarbejdet. De kinematiske ligninger for styregeomatrien bliver fremlagt sammen med de kinetiske ligninger for bevæglese af køretøjet. Sidst valideres den ikke-lineære model ud fra eksperimentæl data, leveret af Danfoss Power Solutions APS.

I kaptitel 3 bliver sensitiviteten af modellen undersøgt, her testes betydningen de ukendte parametre enkeltvis før de bliver estimeret ved hjælp af en optimerings algoritme. Med de optimale parametre for modellen, sammenlignes de simulerede resultater med test dataen fra Danfoss for at vurdere hvorvidt modellem er i stand til at estimere dækkræfternes virkning på styremekanismen.

Kapitel 4 er en sammenfattende diskussion omkring hele projektet. Her disskuteres resultaterne af den ikke-lineære models præcision sammenlignet med den målte data. Desuden disskuteres det, om de antagelser der er lavet i løbet af projektet har en betydelig effekt for projektets konklusion.

Specialet konkluderer at den ikke-lineære model ikke er i stand til at beskrive dækkets påvirkning på styremekanismen med stor præcision.

AALBORG UNIVERSITET
STUDENTERRAPPORT

Department of Energy Technology
Mechatronic Control Engineering
Pontoppidanstræde 111
9220 Aalborg Øst

Title:
Investigation of tire dynamics influence on Articulated Frame Steered Vehicles Steering Performance

Project:
4^{th} semester MCE

Project period:
1^{st} of February to 30^{th} of May 2024

Project group:
Malthe Goosmann

Email:
mgoosm18@student.aau.dk

Supervisor:
Henrik Clemmensen Pedersen

Number of pages:
57

Number of appendices:
5

Finish date:
30^{th} of May 2024

Participants:

Malthe Goosmann

Abstract:

This investigation focuses on the influence of tire dynamics on the steering performance of articulated frame-steered vehicles. Articulated vehicles are advantageous for their maneuverability and off-road capabilities, making accurate simulation models crucial for improving comfort and control. This study develops a nonlinear dynamic tire model to predict the forces acting on the vehicle's steering system, considering tire structure, performance, and dynamic behavior.

The model incorporates kinematics and dynamics of the steering geometry, validated through simulations using data from various operating conditions. Results show that the model can accurately predict low-frequency dynamics, capturing the general behavior of the vehicle during snake test. However, the model struggles with high-frequency oscillations, which are critical for predicting vibrations and other rapid movements that impact driver comfort. Additionally, the model's performance is less accurate under varying inertia conditions, indicating the need for more sophisticated handling of mass distribution and its effects on the vehicle.

Parameter estimation and sensitivity analysis were conducted to optimize the model, revealing that the spring and damping coefficients significantly influence the accuracy of predictions. Despite these efforts, the model demonstrates limitations in fully capturing the dynamic behavior under all tested conditions.

Preface

This master thesis is developed on the fourth semester of the Master programme Mechatronic Control Engineering at Aalborg University by one student. The research was carried out from February 1st to May 31st.

The mathematical model is composed in MATLAB and the extension package SIMULINK as the simulation tool for the project. Dimensions, inertia, and masses are found in a SOLIDWORKDS 3d CAD model.

The author would like to give a special thanks to supervisors Henrik Clemmensen Pedersen and Emil Nørregaard Olesen for constructive feedback and for providing the nessescary data.

Reading Guide

The prerequisites for reading this report are knowledge in dynamics, dynamic modeling, hydraulics, and general engineering terminology. Figures, equations, and tables are named accordingly to the chapter in which they appear, the first figure in chapter one is 1.1 and the second is 1.2 etc. They appear in chronological order in which they are referred. The words Terex and vehicle are used interchangeably, referring to the Terex L310 wheel loader. Moments and torques are also used interchangeably.
The project uses IEEE citations when referring to sources that can be found at the end of the report.
All values are given in SI units unless stated otherwise.

Aalborg University, May 31, 2024

Nomenclature

Symbol	Definition	Unit
α	Angle	$[rad]$
$\dot{\alpha}$	Anglular velocity	$[\frac{rad}{s}]$
$\ddot{\alpha}$	Anglgular acceleration	$[\frac{rad}{s^2}]$
σ	Angle	$[^\circ]$
σ	Stress	$[\frac{\mathrm{N}}{\mathrm{m}^2}]$
γ	Angle	$[^\circ]$
μ_c	Coulomb friction	[]
μ_v	Viscous friction	[]
τ	Torque	$[\mathrm{N} \cdot \mathrm{m}]$
M	Moment	$[\mathrm{N} \cdot \mathrm{m}]$
ω	Angular velocity	$[\frac{rad}{s}]$
ω_n	Natural frequency	[Hz]
A	Area	$[\mathrm{m}^2]$
F	Force	[N]
f	Frequency	[Hz]
k	Spring constant	[-]
B	Damping constant	[-]
L	Length	[m]
m	Mass	[kg]
P	Pressure	[Pa]
t	Time	[s]
J	Inertia	$[\mathrm{kg} \cdot \mathrm{m}^2]$
W	Width	[m]
h	height	[m]
r	Length	[m]
g	Gravitational acceleration	$[\frac{\mathrm{m}}{\mathrm{s}^2}]$
x_c	Cylinder position	[m]
$\dot{x}_c$	Cylinder velocity	$[\frac{\mathrm{m}}{\mathrm{s}}]$
$\ddot{x}_c$	Cylinder acceleration	$[\frac{\mathrm{m}}{\mathrm{s}^2}]$

Subscripts	**Definition**
Cyl	Cylinder
C	Cylinder
COM	Center of mass
T	Tire
fric	Friction
fr	Front right
fl	Front left
rr	Rear right
rl	rear left
L	Left
R	Right
est	Estimated
meas	Measured
ref	Reference
eff	effective
rr	Rolling resistance
hp	High pass
eq	Equivalent

Contents

Introduction 1

In recent years the demand for construction has increased steadily, combined with urban locations that require tight spaces have led to higher demand for articulated, heavy-duty vehicles. This is due to their maneuverability, versatility, and off-road capabilities that prove valuable in challenging terrain. With the increased use of these vehicles, the demand for accurate simulation models becomes important. One of the aspects that are difficult to determine accurately is the influence of tire dynamics, which affects the comfort of the driver and the precision of the vehicle. This is due to vibrations generated at certain frequencies of the tire which moves the vehicle uncontrollably. To reduce these vibrations a tire model can help predict the movement of the vehicle and thereby reduce the discomfort. A tire is a complicated structure as the behavior of the tire is dependent on multiple features such as tire pressure, temperature, road surface, etc; these influence the tire to a greater or lesser extent. [1]

1.1 Motivation

Various types of steering layouts exist for vehicles each with advantages and disadvantages in different areas. In figure 1.1 four steering layouts are presented each with a separate steering layout. These can be divided into two main categories of vehicles, rigid body (a,c,d) and articulated (b). The rigid-body vehicles have a single, fixed chassis that runs the entire length of the vehicle. The articulated vehicle consists of two bodies that are connected around a pivot joint. Each body is connected separately to a wheel axel, by rotating the bodies around the pivot point the vehicle turns. This type of movement results in greater maneuverability due to a smaller turning radius. Another advantage is the ability to keep all four wheels on the ground in uneven conditions as the bodies can flex around the pivot point; with a rigid-body vehicle, it is common to see one or two wheels lift from the ground when navigating an uneven surface. [2]

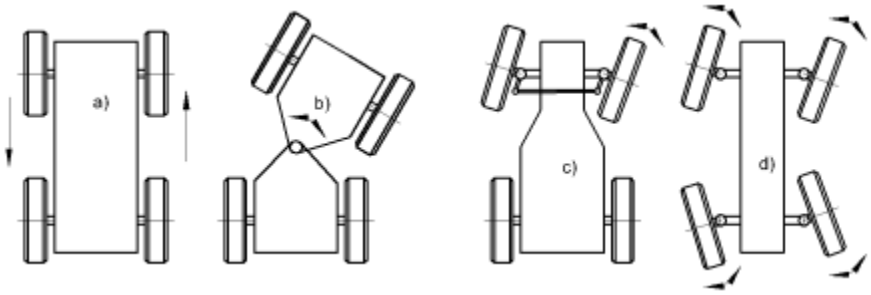

Figure 1.1. Steering of a wheeled vehicle. a) Slip steering; b) articulated steering; c) coordinated steering, d) independent steering [3]

In an articulated vehicle the driver is usually located near the center and the pivot point, this makes the driver exposed to the lateral movement of the vehicle. This essentially means that when the vehicle turns the driver is moved away from the origin point. Figure 1.2 shows how this makes the driver vulnerable to unwanted steering motions in the vehicle. A general problem with the articulated steering layout is a vibrating motion when a turning motion is initialized or stopped also known as jerk. When a driver is exposed to this motion hundreds of times a day this will induce fatigue, reduce performance, and increase the probability of injury or accidents.[1]

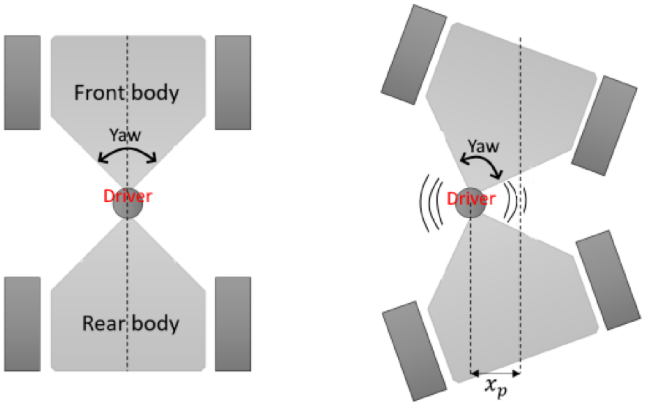

Figure 1.2. Yaw Motion of the articulated vehicle.

As the tires are a contributor to disturbances it is interesting to investigate to what extent a tire model can predict the movement of the vehicle. To do this, a general understanding of a tire and vehicle is necessary as the movement of the vehicle determines the forces on the tires.

1.2 System Description

The Terex L310 Wheel loader used in this paper is used at Danfoss as a test vehicle for multiple purposes. This 17.6 ton Wheel loader is produced by AtLAS GmbH in Germany with the purpose of being a mid size versitile loader. Figure 1.3 shows the Terex L310 in a top and side view with corresponding dimensions and the standard bucket as attachment.

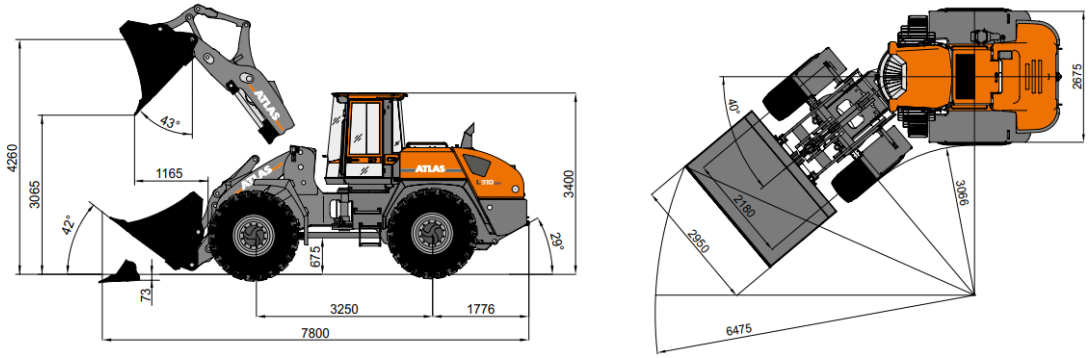

Figure 1.3. Top and side view of the Terex L310 Wheel Loader including dimensions and angles. Dimensions are in mm.

The wheel loader is mounted with the 23.5R25 VJT L3 Bridgestone Radial Loader Tires, the specifications can be seen in figure E.1 in appendix E. The vehicle can be operated in two drive modes, namely slow drive which operates from 0-6 km/h, and fast driver which operates from 0-40 km/h. From the right side of figure 1.3 the max steering angle can be found to be ±40° to either side. The steering geometry of the wheel loader consists of 2 bodies, the revolute joint and 2 hydraulic cylinders connected in parallel with the front and rear body. The hydraulic steering system consists of a variable displacement pump, a priority valve, a hydrostatic steering unit, pressure relief valves, and anti-cavitation valves.

1.2.1 Tire Structure

The structure of the radial loader tire will be examined to understand the internal dynamics of the specific tire. The general layout of a tire on a rim is shown in figure 1.4.

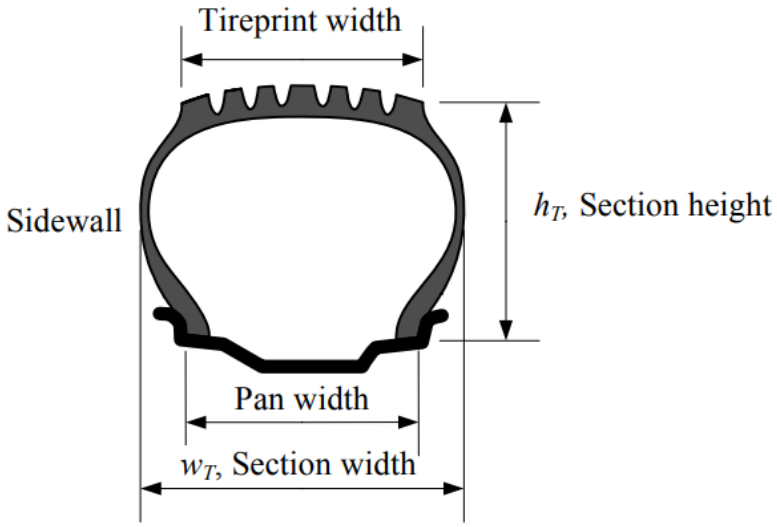

Figure 1.4. Cross section of a tire on a rim to show tire height and width. [4]

The tireprint is the only contact point with the road which means all force from the vehicle to the road is transfered through the tireprint. The section width (w_T) is the width of an unloaded tire. The section height (h_T) in addition with the the rim hight sums to the total wheel radius.
As the name suggests the tire on the wheel loader is a radial tire where a general radial tire structure is shown in figure 1.5. From the inside the inner liner is the rubber base of the tire that forms the inside of the tubeless tire, on top of this is the carcass which is the main structural part of the tire, absorbing most of the shock and load, essentially the carcass determines the structure of the tire. In figure 1.5 it can be seen how the plies are perpendicular to the forward movement of the tire which is how a radial tire is defined. The bead bundle is a high-strength steel cable, this makes sure the connection with the rim is stable and the force transfer is uniform. Belt buffers are rubber-coated steel that ensures uniform contact with the road, belt buffers can be placed in layers to provide more strength to the tire. The inner layer are created from polyester cords that provide the tire with directional stability, these are usually laid down crosswise that forms a strong pattern. The final parts are the sidewall and tread, the sidewall provides stability in the lateral direction and reduces risk of puncture, the tread is the contact point with

the surface and have a specific design depending on multiple factors eg. weather or load. [4]

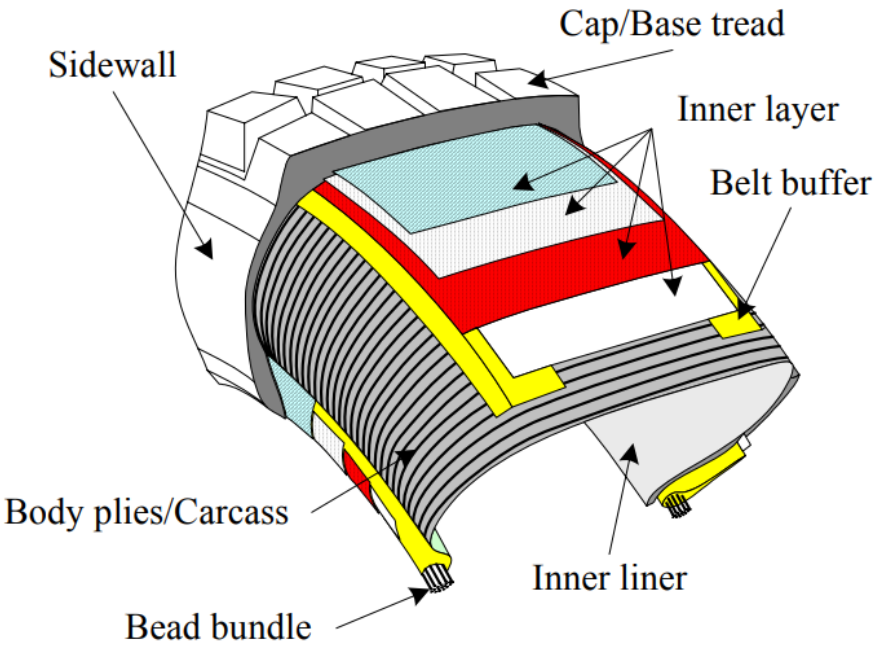

Figure 1.5. Illustration of a sample radial tire interior components and arrangement. [4]

The other type of tire that is usually used is the bias tire where the difference being in the pattern of the carcass. The bias tire has a diagonal pattern that can be seen in appendix B. When comparing the two types of tire structure the flexibility of the tread under load is the main difference. the bias tire flexes in the longitudinal direction meaning the tire will have a longer contact area wheras the radial tire flexes in the lattitudal direction creating a wider contact area. The wider contact area results in more grip on the contact surface and ensures more uniform tire wear. This is shown in figure 1.6, where the radial tire flexes more in the sidewall, effectively keeping the large tire-ground contact while the bias tire looses grip in the edge of the tire-ground contact area.

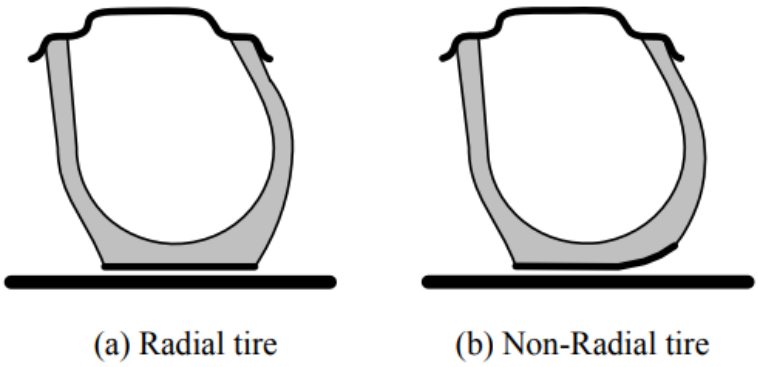

Figure 1.6. Ground-sticking behavior of radial and non-radial (bias) tires in the presence of a lateral force. [4]

1.2.2 Tire Performance

The performance of truck tires is influenced by a varity of factors. These factors can be broadly classified into tire characteristics, road surface conditions, environmental factors, and dynamic influences.

Tire characteristic Tire characteristics include tread design, composition, and inflation pressure. If chosen correctly these parameters ensure grip on the working surface together with a minimal fuel consumption. These parameters are all changeable before operating the vehicle which should be taken into consideration for optimal performance

Road conditions and environmental factors The surface influences the traction of the tire where a firm rough texture is preferred to a loose soft surface. Poor road conditions can lead too increased wear, higher fuel consumption and lower traction. In cold or wet weather, ice or wet surfaces can significantly reduce the traction and precision of the vehicle.

Dynamic influences Changes in the load of the truck causes the center of mass to move and thereby the tire parameters to change. This results in different normal forces for each tire which correlates to the contact area with the ground. Each tire can experience different normal forces when the load changes and the vehicle turns.
The dynamics of a tire is further discussed in the next section.

1.3 Tire Dynamics

The tire is the only part of the vehicle in contact with the ground during operation. In figure 1.7, a coordinate system is placed at the center of the tire-road interaction. The tire is represented by a flat disk in the tire plane, the x-axis runs parallel with the tire plane representing the forward and backward movement of the tire also called the longitudinal axis. The y-axis is perpendicular to the x-axis, which represents the latitudinal axis, and the z-axis is the vertical axis and is perpendicular to the ground plane. The angle α is the sideslip angle which is defined as the angle between the vehicle's longitudinal direction and the traveling direction of the vehicle's center of gravity. The camber angle γ is the angle between the tire plane and the vertical plane. [4]

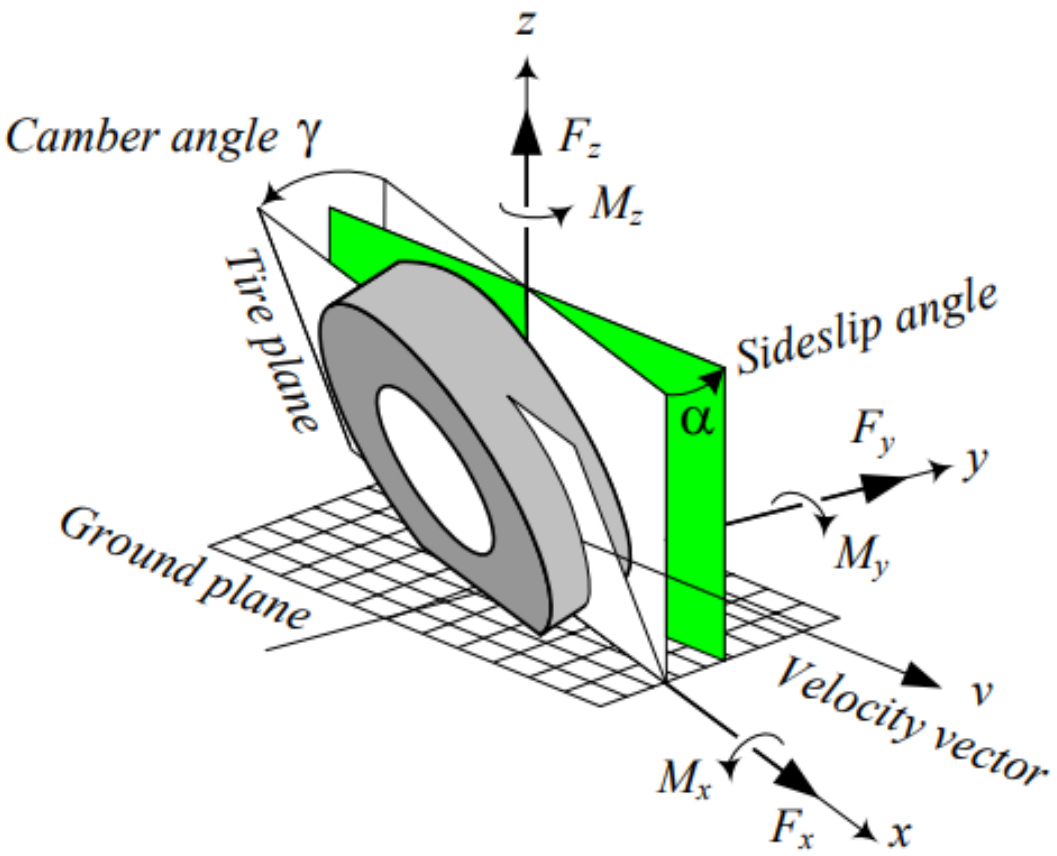

Figure 1.7. Tire coordinate system. [4]

When the vehicle maneuvers it forces the tire to deflect producing forces acting from the ground on the tire, from figure 1.7 these forces are:

- F_x is the longitudinal force acting when accelerating or braking
- F_y is the lateral force acting when the tire is turning
- F_z is the vertical force due to the weight of the vehicle
- M_x is the roll moment causing the tire to tilt, this produces the camber angle γ
- M_y is the pitch moment causing the tire to move forward og backward, also called rolling resistance torque
- M_z is the yaw moment causing the tire to turn about the z-axis.

The tire deflection occurs in all (vertical, longitudinal, lateral) directions when the tire is moving. The deflection amount depends on the load applied and the tire stiffness in the given direction. Tire parameters are usually found experimentally as the complex structure of tires makes it hard to predict the exact behavior.

1.3.1 Stress

When the tire sits on the ground the stress is divided across the contact patch with the ground. Looking at the forces on the tire the normal stress distributions can be described by

$$\sigma_z = F_z/A \tag{1.1}$$

where F_z is the force in the z direction and A is the tire print area. According to [4] the tire print area can be described as $\frac{x^{2n}}{a^{2n}} + \frac{y^{2n}}{b^{2n}}$ where a and b are the tire dimensions, for radial tires n = 3 or n = 2. The normal stress distribution acts uniformly on the tire print as shown in figure 1.8a, this is expected since the tire is stationary and the only force is the normal force. When the tire is moving in a forward direction, rolling resistance is introduced. The deformation pushes the stress to the front of the tire as shown in figure 1.8b.

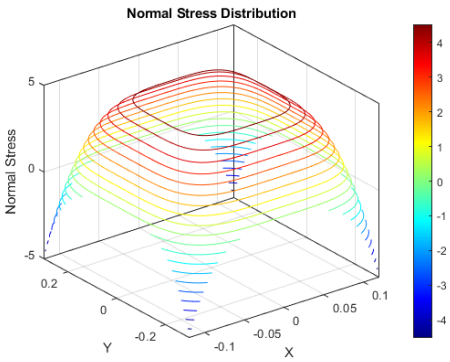

(a) 3D Normal stress distribution

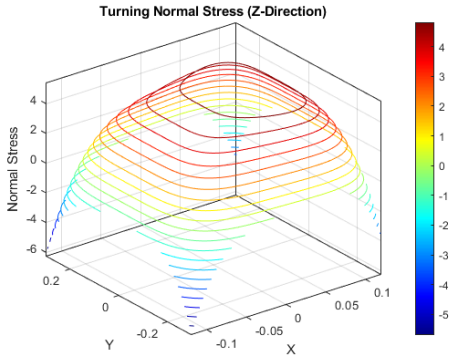

(b) 3D Normal stress distribution when rolling

The tangential stresses of the tire in the x and y directions act similar but opposite to each other. They can be described by equation (1.2)

$$\sigma_{x/y} = \mu_{x/y} \cdot F_z \tag{1.2}$$

In x direction, the tire tries to stretch the ground meaning that the forces work from outside towards the inside. In the y direction the tire compacts the ground working from the inside to the outside. The stress distribution are shown in figure 1.9a and 1.9b, here it can be seen how the stresses acts in similar but in different directions. These distributions are not constant as they depend on the structure of the tire, surface structure, inflation pressure, wear, ambient temperature, etc. [4]

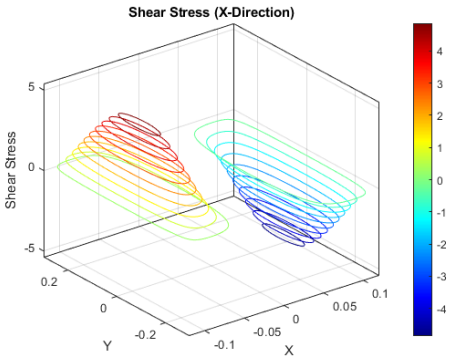

(a) 3D sheer stress distribution in x-direction

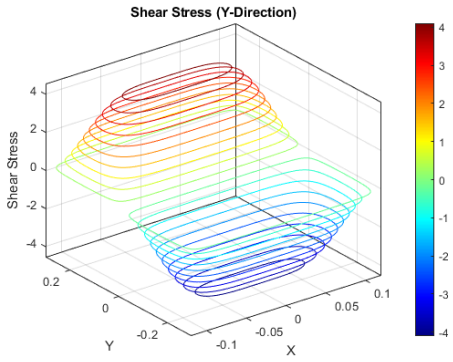

(b) 3D sheer stress distribution in y-direction

These phenomenons combine to rolling resistance which is a measure of the force opposite to the moving direction, rolling resistance can be described by

$$F_r = \mu_{rr} \cdot F_z \tag{1.3}$$

where μ_{rr} is the rolling friction coefficient and F_z is the normal force. From the equation it is clear that the rolling resistance force is proportional to the normal force on the tire. The parameter μ_{rr} depends on various factors such as speed, temperature, inflation pressure etc. [4]

1.3.2 Hysteresis

Hysteresis is a phenomenon in the dynamics of radial tires, manifesting as a lag between applied forces and deformations. Hysteresis occurs due to the viscoelastic tire structure. Viscoelastic materials have both viscous and elastic characteristics when undergoing deformation. This leads to a distinctive behavior where the path followed during loading (when the force is applied) is different from the path followed during unloading (when the force is removed). This phenomenon can be seen in figure 1.10.
When a radial tire rotates under load, it continuously undergoes deformation cycles. As the tire deforms, energy is expended as heat due to internal friction within the material. This energy dissipation is responsible for the difference in energy between the loading and unloading cycles.
The primary consequences of hysteresis in radial tires include increased rolling resistance and heat generation. Rolling resistance affects the performance of the vehicle, as more energy is required to maintain the velocity.[4]

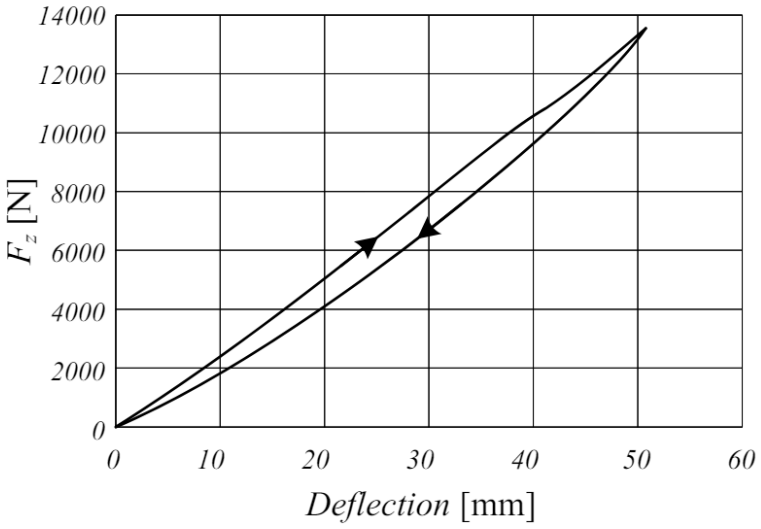

Figure 1.10. Loading and unloading curves of a radial car tire. [4]

1.4 Litterature study

With the tire being impactful on the overall experience of a vehicle it has been in the scope of researchers for more than 50 years. Due to the high complexity the initial tire models were purely emperical but as technoligy evolved, more physical parameters were introduced in the models. The three approaches to developing a tire model are presented below.

Emperical Modeling Empirical tire models are based on experimental data that is interpolated to find the needed parameters. The most commonly used tire model is the

Magic Formula presented by [5] in 1989. This model uses the vertical load, tire slip angle, longitudinal slip, and camber angle to accurately predict the longitudinal force, side force, and self aligning torque One issue with this type of models is the lack of physical interpretation as the parameters are completely determined from interpolation. The Magic Model is still the cornerstone of tire modeling and is widely used throughout the industry.

Physical-Based Modeling The physical approach involves modeling the tire as a system to represent the internal mechanics of the tire including eg. tread deformation, and rubber properties. These models are complex and detailed which results in high accuracy and large computational cost. As the tire is a complex system to describe, the author of this paper was not able to find a purely theoretical model as all use empirical values to some extent.

Semi-Emperical Modeling Semi-empirical models have been developed to decrease the uncertainties from experiments but reduce the complexity of the physical-based models. The basic structure and mathematical formulations are often based on observed tire behavior and experimental data, similar to purely empirical models. Key physical aspects of the tire are accounted for by incorporating principles from mechanics. The F-Tire model presented in [6] showed good accuracy with minimal computational cost when driving over single obstacles at various speeds.
In table 1.1 an overview of the 3 model types is presented for simplification.

Feature	**Empirical**	**Semi-Empirical**	**Physical**
Complexity	Low	Moderate	High
Accuracy	Lower	Moderate	High
Physical interpretation	Limited	Moderate	High
Data requirements	High	Moderate	High
Suitable for	Basic simulations Performance analysis	Higher accuracy simulations Broader analysis Understading internal forces	High accuracy analysis Understading underlying physics
Computational Cost	Low	Moderate	High

Table 1.1. Comparison of different modeling types.

What most tire models have in common is that they are developed on data from a hard, flat surface. When driving on soft ground or bumpy roads the tire becomes an important element in the suspension system of the vehicle. Since [6] showed capability to accurately predict the tire force accurately when driving over obstacles [7] suggested that Ftire is the only viable commercial tire model when driving "off-highway".

State of the Art Recent advancements have focused on developing physical-based models with parameter identification techniques to predict whole-body vibrations in vehicles. In [7], the impact of whole-body vibrations on an articulated dump truck was examined,

focusing on predicting how the tires affect the vehicle's vertical dynamics. Using a physical-based method and parameter identification for the tire properties [7] derived a model with three parameters that can predict the vertical movement and acceleration of the driver with high accuracy.
In recent years machine learning have been introduced to the tire modelling world, using an accelerometer attached to inner liner of a tire that collected the acceleration in x, y, z direction [8] was able to train a neural network using machine learning to estimate the lateral, longitudinal, and vertical tire forces with errors below 5%.

With these considerations the following section will outline the problem statement of the project.

1.5 Problem statement

Objective

This paper's objective is to develop a physical-based tire model that accurately predicts forces acting on the Terex wheel loader. The model should aim to use non-excessive information about the tire and surface and minimize computational effort. The physical approach makes this more applicable for differentiated vehicles compared to the empirical method, as this is based on the physical dimensions of the individual vehicle. This model should be able to calculate the forces on the individual tires as the vehicle operates with and without load.
The model will be developed to fit a 17.6-ton L310 Wheel Loader fitted with 23.5R25 Bridgestone VJT Radial Loader Tire as shown in section 1.2.

Problem statement

Is it possible to develop a lumped nonlinear dynamic tire model that can predict the influence of the tire on the Terex L310 steering system?

Modeling 2

To accurately determine the tire influence on the vehicle a dynamic model of the combined system is necessary. The inputs to the tire model include the angle, angular velocity, and angular acceleration for the tire and the rim. The overall model strategy is shown in figure 2.1, the system requires a cylinder input and outputs the pressure difference in the cylinder chamber.

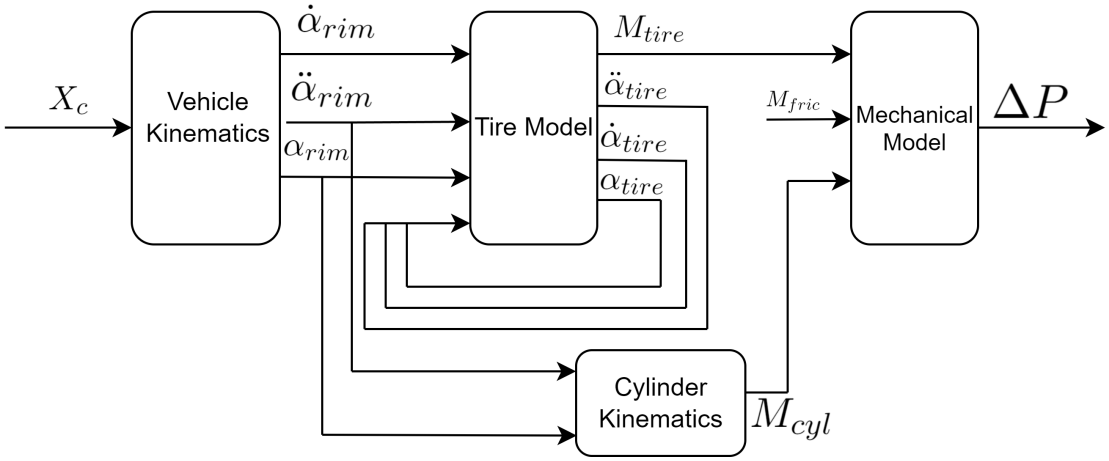

Figure 2.1. Overall model strategy

2.1 Kinematics

The steering system of the Terex pivots around the centerpoint which creates varying angles for and lengths of the cylinders. The steering system is sketched in figure 2.2 with all of the required lengths shown.

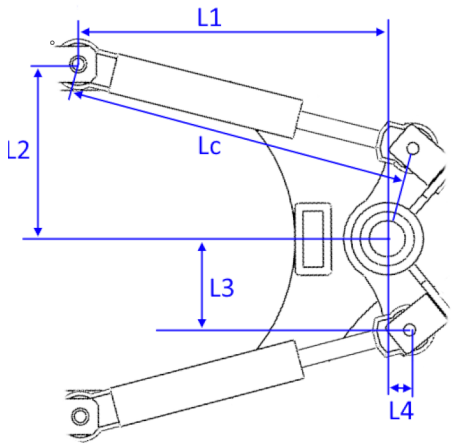

Figure 2.2. Lengths on steering mechanism of Terex.

The kinematics of the steering system is investigated by looking at one of the two cylinders, when no steering occurs the system is at rest position with steering angle α_0. When the linear cylinders extend or retract this introduces an updated steering angle dependent on the steering input from the cylinder x_c. The extension of each cylinder is 330mm going from full steering left to full steering right. When the vehicle moves in a straight line the cylinder extension is determined to be 0 resulting in a range of $\pm 165mm$. A trigonometric illustration of the system is shown in figure 2.3, the steering angle depends on the relationship between the constant lengths L_c, L_1, and L_0.

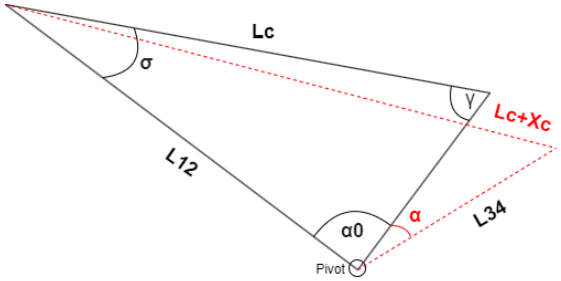

Figure 2.3. Steering kinematics

The steering angle α and the angles σ and γ are defined as in equations (2.1) to (2.3).

$$\alpha = \cos^{-1}\left(\frac{L_{12}^2 + L_{34}^2 - (L_c + x_c)^2}{2 \cdot L_{12} \cdot L_{34}}\right) - \alpha_0; \tag{2.1}$$

$$\sigma = \cos^{-1}\left(\frac{(L_c + x_c)^2 + L_{12}^2 - L_{34}^2}{2 \cdot L_{12} \cdot (L_0 + x_c)}\right); \tag{2.2}$$

$$\gamma = 180 - (\alpha + \sigma); \tag{2.3}$$

The range of motion for the steering angle α is plotted with a sine input ranging from -165mm to +165mm on figure 2.4. It is observed the range of motion is ± 40 degree as expected.

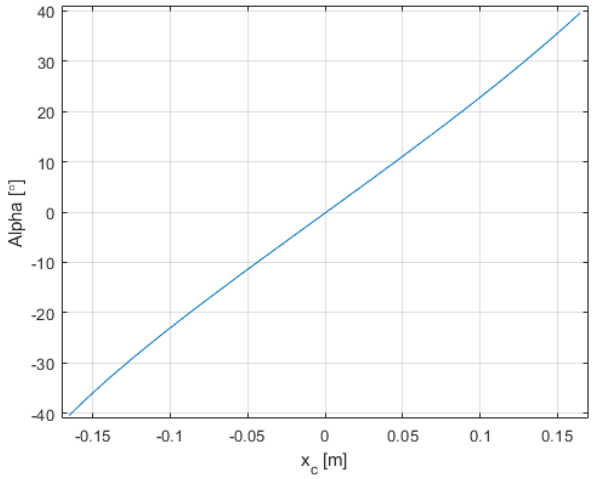

Figure 2.4. Steering range of motion

2.2 Dynamic model

The dynamic model is developed using the kinematic equations to derive the forces acting on the steering cylinder.

Forces on cylinder To obtain a dynamic model the vehicle forces are investigated in an instance of a right turn. Due to the viscoelastic properties structure of the tire, they create a reaction force in the opposite direction of the force of the turn. This is shown in figure 2.5 where the forces of a single tire turning right are illustrated.

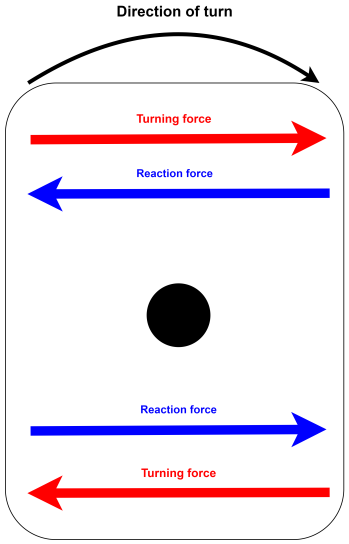

Figure 2.5. Tire force seen from above

The reaction force can be described with a spring and damper system (equation (2.4)) as this resembles the movement of a tire.

$$\tau_{tire} = (\alpha_{rim} - \alpha_{tire}) \cdot k_{tire} + (\dot{\alpha}_{rim} - \dot{\alpha}_{tire}) \cdot B_{tire} - \tau_{fric} \tag{2.4}$$

Where k_{tire} and $B_{tire}$is the spring and damper coefficient of the tier, τ_{fric} being the friction between the ground and the tire. The friction is described in equation (2.5)

$$\tau_{fric} = \mu_c \cdot 2 \cdot L_{eff} \cdot \frac{m_{terex}}{4} \cdot g + \mu_v \cdot \dot{\alpha}_{tire} \tag{2.5}$$

Where μ_c is the coulomb friction constant, L_{eff} is the crossectional length of the contact patch, and μ_v is the viscous friction constant.
The angular velocity is needed to obtain τ_{tire}, this can be found by taking the derivative of equation (2.1)

$$\begin{aligned} \dot{\alpha}_{rim} &= \frac{d}{dt} cos^{-1}\left(\frac{L_{12}^2 + L_{34}^2 - (L_c + x_c)^2}{2 \cdot L_{12} \cdot L_{34}}\right) - \alpha_0 \\ \dot{\alpha}_{rim} &= \frac{2 \cdot (L_0 + x_c)}{L_{12} \cdot L_{34} \sqrt{1 - \frac{(L_{12}^2 + L_{34}^2 - (L_0 + x_c)^2)^2}{4 \cdot L_{12}^2 \cdot L_{34}^2}}} \cdot \dot{x}_c \end{aligned} \tag{2.6}$$

The general block diagram for a the mass spring damper system is shown in figure 2.6. When driving the vehicle each wheel has its own system with individual forces acting.

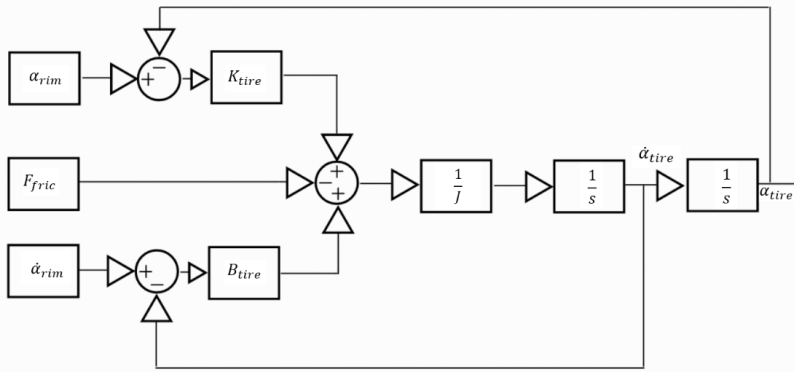

Figure 2.6. Mass spring damper system

The spring and damper coefficients are modeled such that they depend on the angle of the rim when turning. The front left and rear left is assumed to experience the same angular displacement while the right side tires experience the opposite. The spring and damper for the left and right side are modeled as in equation (2.7)

$$\begin{aligned} K_L &= K_0 + \alpha \cdot K_1 \\ B_L &= B_0 + \alpha \cdot B_1 \\ K_R &= K_0 - \alpha \cdot K_1 \\ B_R &= B_0 - \alpha \cdot B_1 \end{aligned} \tag{2.7}$$

Where k_L, B_L, and k_R, B_R are the left and right side coefficients, respectively.
The tire torques acts on the center of the tire as illustrated on figure 2.5. Combining the four tire moments using superposition (equation (2.8)) yields one tire moment (M_{tire}) as shown in figure 2.7

$$M_{tire} = \sum_{i=1}^{4} M_{tire,i} \tag{2.8}$$

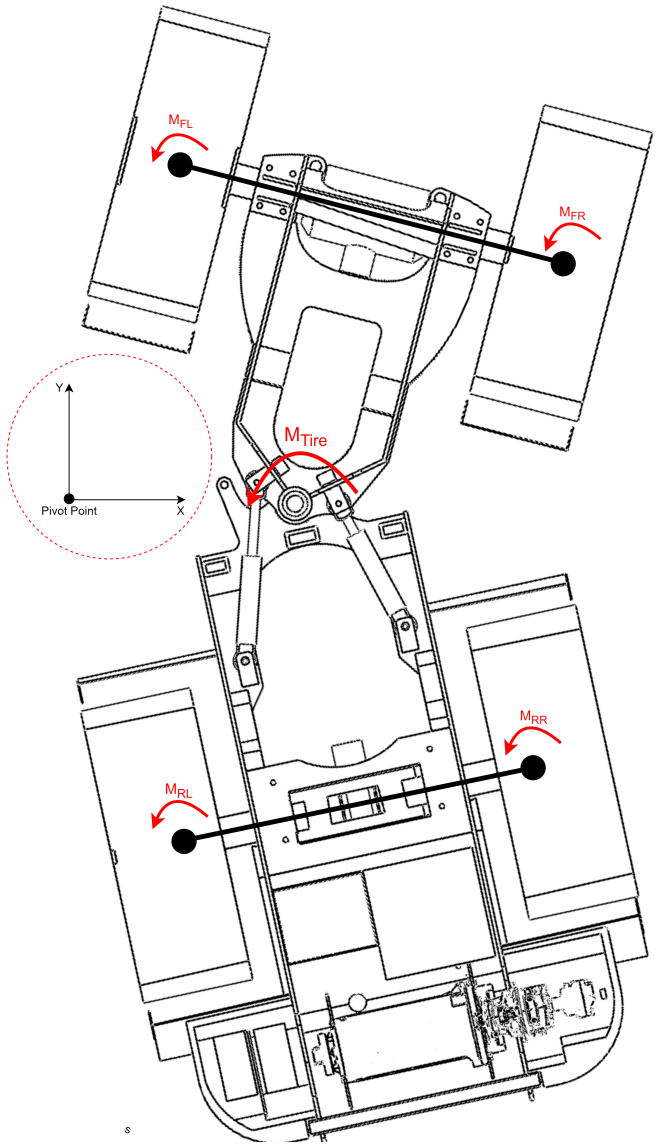

Figure 2.7. Direction of tire torques

The direction of the individual forces created by the cylinder on the tire acts as in figure 2.8a. The forces are determined to be positive when the cylinder is extending. The cylinder moment is calculated using a moment balance around the pivot point as shown in figure 2.8b where the three acting moments with direction are determined.
Setting up the moment balance around the pivot point yields

$$M_{cyl} = J_{eq} \cdot \ddot{\alpha}_{rim} + M_{tire} + M_{fric} \tag{2.9}$$

where J_{eq} is the equivalent inertia around the center of mass and M_{fric} is a combined coulomb and viscous friction. $\ddot{\alpha}_{rim}$ is found by filtering $\dot{\alpha}_{rim}$ with a high pass filter, essentially finding the derivative. The cutoff frequency of the high pass filter will be determined when the dynamics of the vehicle have been analyzed; the general formula for a high pass filter is shown in equation (2.10).

$$G_{hp} = \frac{s}{\tau \cdot s + 1} \tag{2.10}$$

The inertia is obtained from the provided Solidworks model, where the lifting cylinder is extended by 185mm. This position is chosen because the validation data mostly uses this position. From this, the individual cylinder forces are found using the kinematics found in section 2.1.

$$F_{fl} = \frac{M_{cyl}}{\sin(L_{34})} \tag{2.11}$$

$$F_{fr} = \frac{M_{cyl}}{\sin(L_{34})} \tag{2.12}$$

$$F_{rr} = \frac{M_{cyl}}{\sin(L_{12})} \tag{2.13}$$

$$F_{rl} = \frac{M_{cyl}}{\sin(L_{12})} \tag{2.14}$$

Since the cylinder forces and the area inside the cylinder are known, ΔP can be derived

$$\begin{aligned} \Delta P_l &= \frac{F_{fl}}{A_B} + \frac{F_{rl}}{A_A} \\ \Delta P_r &= \frac{F_{fr}}{A_B} + \frac{F_{rr}}{A_A} \end{aligned} \tag{2.15}$$

where $\Delta P = P_R - P_L$. The pressure difference in both chambers is assumed to be equal, $\Delta P_l = \Delta P_r$

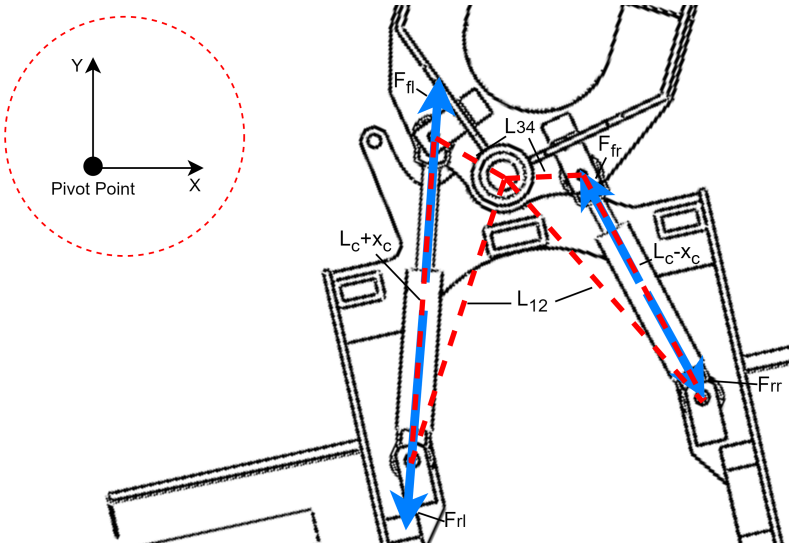

(a) Direction of tire forces projected to hydraulic cylinders

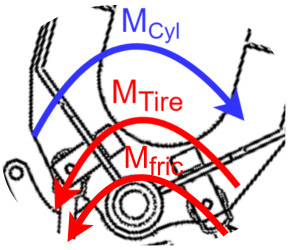

(b) Moment balance around pivot point

Figure 2.8

The pressure in the cylinder is connected in cross parallel with each other meaning the rod side of the left cylinder is connected with the chamber side of the right cylinder and vice versa. The connection is shown in figure 2.9, here it can also be seen how the forces from the tires affect the cylinders. Assuming that the center of gravity is located directly on top of the pivot point, the tire forces can be split into left and right where it is assumed the forces are distributed evenly on the cylinders.

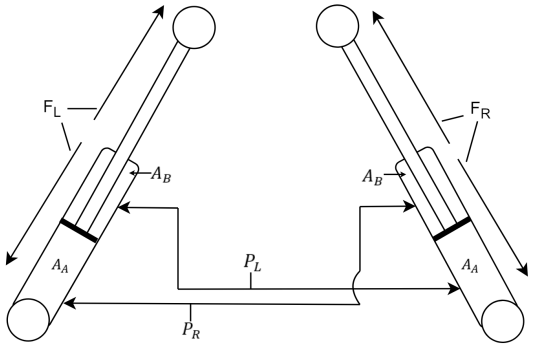

Figure 2.9. Forces acting on cylinder

Having established a lumped parameter dynamic model the next step is to validate this using experimental data.

2.3 Model Validation

The model validation is done using data provided by Danfoss, the data is made from experiments with variable situations, the reference being a snake test with 0.2Hz frequency, no load in the bucket, 4 bar tire pressure, lifting cylinder extended 185mm, and driving on gravel. The test data have some deviation in the amplitude for the first period. When validating the model this data is ignored, as this can be due to various parameters which is hard to determine without further investigation. The cylinder input to the model is a sine wave with an amplitude of $\pm 0.165m$ and frequency of 0.2Hz; this is shown in figure 2.10, which yields a steering angle of $\pm 40°$.

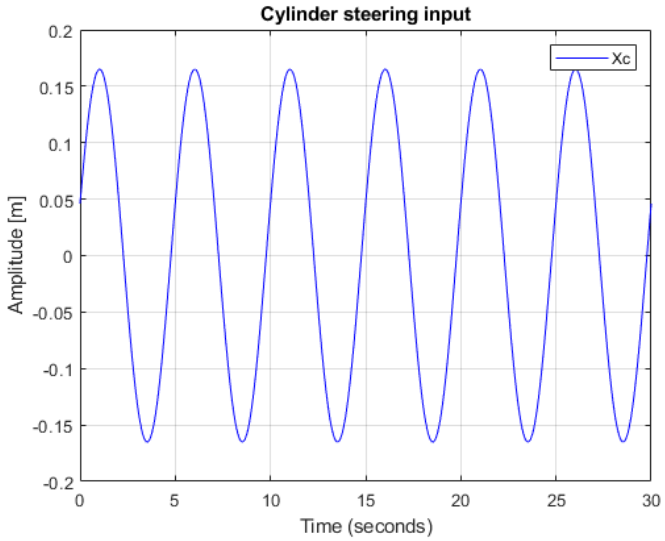

Figure 2.10. Steering cylinder input

To determine the cutoff frequency of the high pass filter the frequency response of the angular velocity is analysed in figure 2.11. Here it can be observed that the dominant frequency is at 0.2Hz as expected and the smaller contributions are below 1.5Hz. The cutoff frequency is placed well above this at 5Hz. This yields $G_{hp} = \frac{s}{0.032 \cdot s + 1}$.

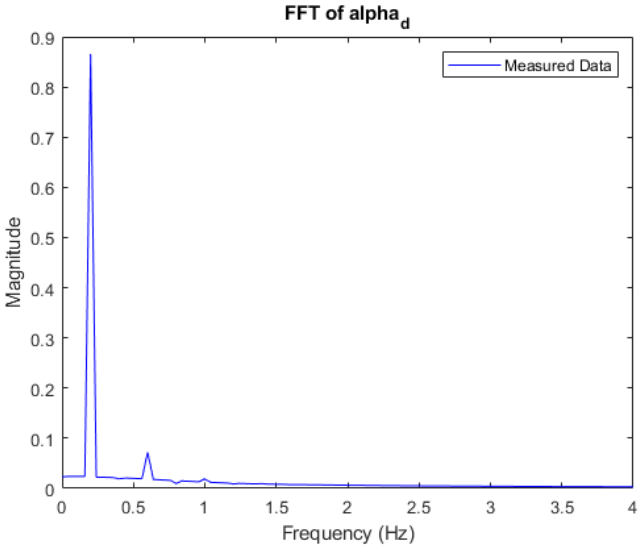

Figure 2.11. Fast fourier transform of the angular velocity

The initial test in figure 2.12 shows the model is able to capture the slow dynamics of the pressure difference between the chambers but lacks capability in the high-frequency area. The lower frequency pressure changes come from the vehicle dynamics, while the high frequency possibly stems from the tires. The dominant moment in the pressure difference is the vehicle dynamics, which is also the case in the dynamic model. The overall development of the oscillations is the same for the measured and the simulated, with a high amplitude when the vehicle is turning fast, which reduces as the vehicle reaches its maximum turning angle. This test is conducted with $k0_y = 15000, k1_y = 5000, b0_y = 150, b1_y = 50$.

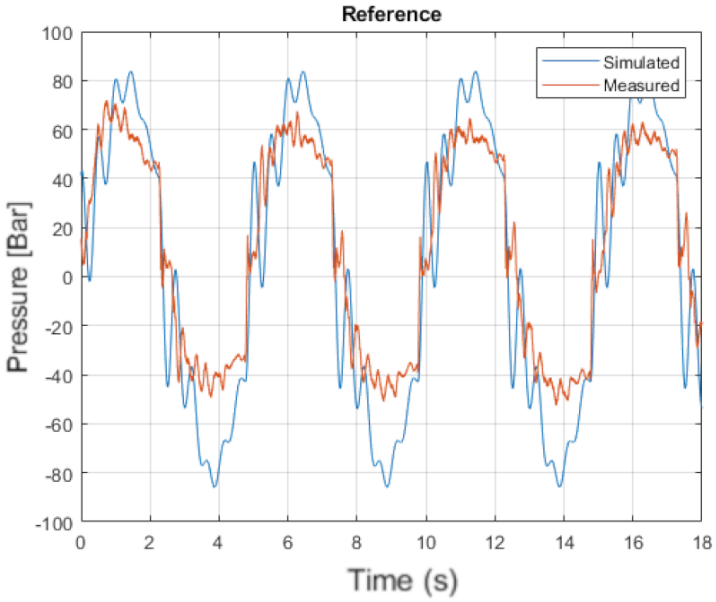

Figure 2.12. Initial ΔP test

The higher frequency oscillations may occur due to vibrations from the tire. To check whether this is true, the eigenfrequency of the tire is compared with the frequency of the oscillations. The eigenfrequency of the simulated tire is found by equation (2.16) to be

$\approx$ 2Hz with the initial value of K = 15000.

$$\omega_n = \frac{1}{2 \cdot \pi} \sqrt{\frac{k}{J_{tire}}} \tag{2.16}$$

The oscillations mostly occur when $\dot{\alpha}$ is large, meaning the vehicle turns fast. Zooming in on one of the peaks (figure 2.13) it is observed the period of the oscillations is around 0.2s, which yields a frequency for the tires of 5Hz.

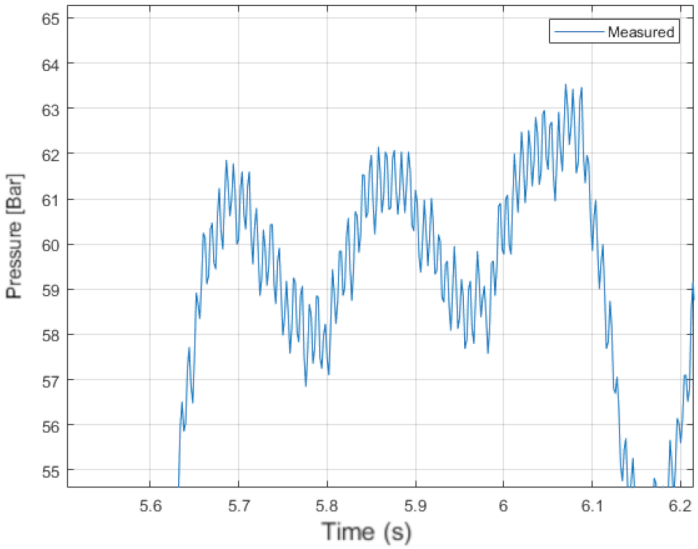

Figure 2.13. Zoomed view of reference data

The reference data includes many frequencies whereas the simulation model is more restricted. Using a FFT analysis to investigate how well the dominating frequencies match in figures 2.14a and 2.14b it can be seen that both dominating frequencies lies around 0.2Hz. The reference data has smaller peaks at around 1.2, 4.5, and 5.5Hz, where the simulated data have a minor peak around 0.8 and 3Hz. The magnitude of the minor peaks is roughly the same. The magnitude of the main peak at 0.2Hz is three times larger for the simulated model.

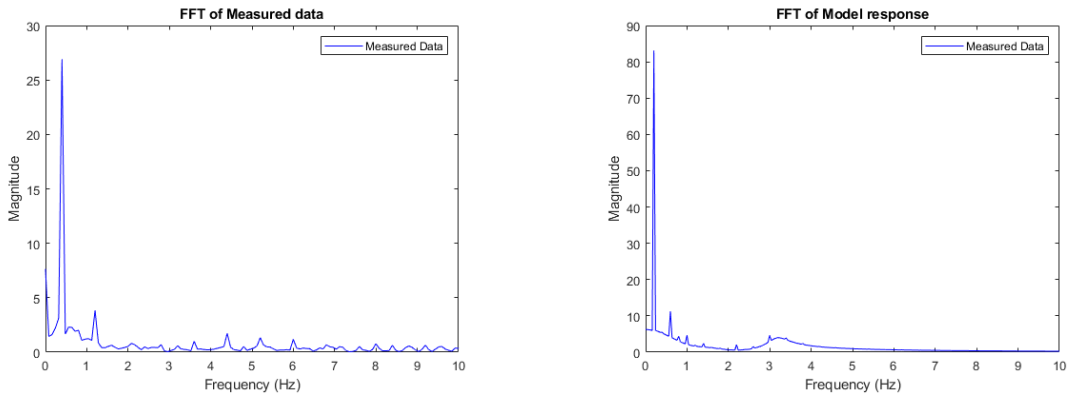

(a) FFT of validation data ***(b)*** FFT of simulated model response

Figure 2.14

In general, the dynamic model is able to replicate the dominant dynamics of the vehicle, although with limited precision.

Parameter Estimation 3

With the simple dynamic model validated in the low-frequency range, there are multiple unknown parameters, this includes the k and B values for each tire and the friction coefficients. Initially, these are not separated from each other, meaning each tire shares the same values for these parameters. The friction coefficients depend on tire characteristics such as tread pattern, tire pressure, road conditions, internal temperature, and weather conditions. These parameters are considered constant since the tests conducted in this project are less than 1 minute long.

3.0.1 Sensitivity Analysis

The effect of each unknown parameter is tested individually in a sensitivity analysis. To perform this, each parameter has been varied to observe the behavior on ΔP compared with the initial value. The full results can be seen in appendix C, in figures 3.1a, 3.1b, 3.2a and 3.2b, a peak is investigated further because the high-frequency oscillations occur mainly at the peaks. It can be observed that lowering the constant spring stiffness increases the amplitude of the oscillations and lowers the vehicle frequency while lowering the angular-dependent spring stiffness decreases the overshoot. Increasing the constant dampening factor lowers the amplitude and increases the frequency of the oscillations. The same is observed for the angular-dependent dampening, though to a lesser extent.

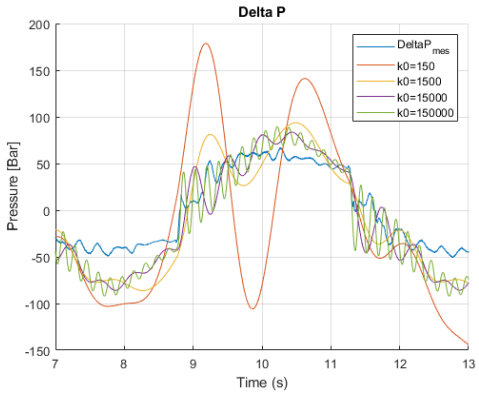

(a) Affect of k0 on ΔP

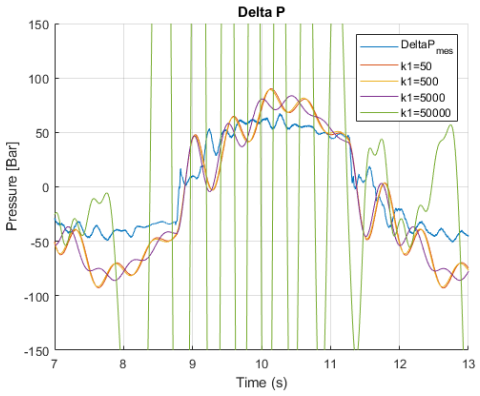

(b) Affect of k1 on ΔP

Figure 3.1

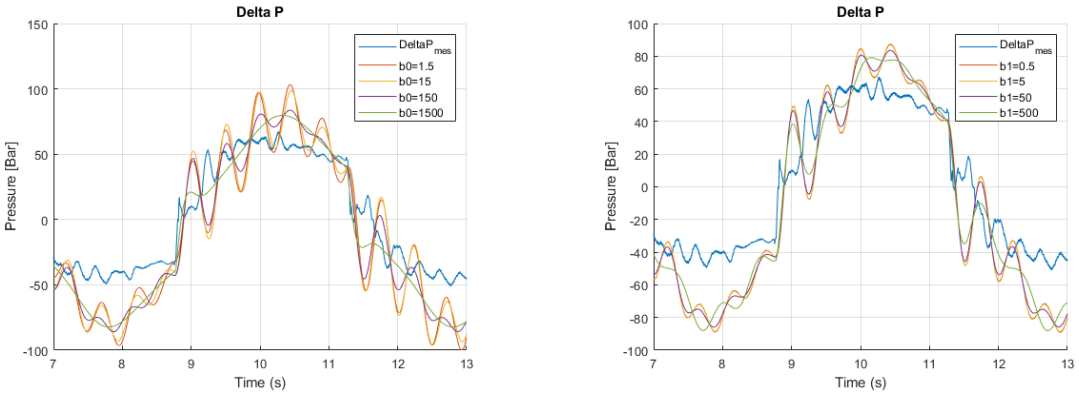

(a) Affect of b0 on ΔP

(b) Affect of b1 on ΔP

Figure 3.2

This could indicate that the angular-dependent spring coefficient should be increased to capture the dynamics better. With these observations, it is possible to estimate the values for each parameter to mimic the dynamics more accurately.

3.0.2 Parameter Estimation

Since the model shows the ability to predict the pressure difference, the spring and damper parameters are estimated to obtain optimal values. The optimum values of the four parameters are estimated to lie within the tested values in the sensitivity analysis. The optimized values are determined using a sequence of simulations where the parameters vary and all possible combinations are tested. The tests are divided into multiple rounds to reduce the computational power needed. To obtain a general understanding, the increments are large in the first test, reducing as the error reduces. After each iteration, the tests are compared using the sum of squared error (SSE) which is calculated as in 3.1. The initial testing scheme can be seen in table 3.1, and the rest can be found in appendix D.

$$SSE = \sum_i (y_i - \hat{y}_i)^2 \tag{3.1}$$

where y_i is the measured data and $\hat{y}_i$ is the simulated data.

	$k0\_y$	$k1\_y$	$b0\_y$	$b1\_y$
Initial value	7000	1000	50	10
Increment	10000	5000	100	50

Table 3.1. Values of $k0\_y$, $k1\_y$, $b0\_y$, and $b1\_y$ for test 1

For test 1, the lowest SSE was obtained with the parameters set as in table 3.2, this yields the response shown in figure 3.3a. The slow dynamics overshoot the measured data by around 30 bar, which indicates that the dynamics from the vehicle are not accurate. From a zoomed view figure 3.3b, it can be seen that the fast oscillation shares a similar behavior with the measured data, where the amplitude of the oscillations reduces as the angle reaches maximum. The simulated fast oscillations have a frequency of around 2.5Hz, close to the desired 5Hz.

$k0\_y$	$k1\_y$	$b0\_y$	$b1\_y$
27000	1000	250	10

Table 3.2. Optimal values of $k0\_y$, $k1\_y$, $b0\_y$, and $b1\_y$ for case 1 test 1

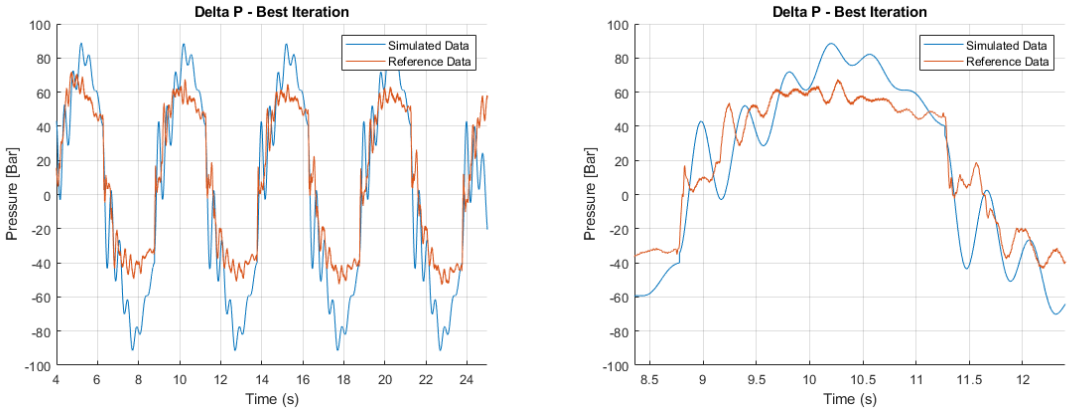

(a) Case 1 test 1

(b) case 1 test 1 zoomed view

Figure 3.3

Since the error is significant, further tests have been performed. All the test parameters and results are presented in appendix D. The lowest SSE was found with the highest tested value for $k0_y$ and $b0_y$ and lowest values for $k1_y$ and $b1_y$. Therefore, test 2 uses higher initial values for $k0_y$ and $b0_y$ while for $k1_y$ and $b1_y$ the initial value and increments are reduced. Test 3 investigates the opportunity for the variable spring and damper to be the dominant force. Test 2 resulted in a 0.25% improvement while test 3 resulted in a 2.9% increase. All tests showed the same behavior, with the peak values becoming $\approx$ 30% larger than the measured data. To avoid this, two other cases were conducted with different friction coefficients. The second case has a reduced $\mu_{c,terex}$, while the third case has a reduced $\mu_{c,tire}$. Table 3.3 compares all simulations. Lowering $mu_{c,terex}$ and $mu_{c,tire}$ reduces the SSE by $2-5\%$ and $27-29\%$ respectively.

test|case	**1**	**2**	**3**
1	—	4.8%	29%
2	0.25%	5%	29%
3	-2.9%	1.9%	27%

Table 3.3. Comparison of SSE for all tests

The most accurate test results from case 3 test 1 and case 2 test 2 are displayed in figures 3.4a and 3.5a with the optimized values as shown in table 3.4 and 3.5. The low k and high b values in case 3 eliminated the high-frequency dynamics in the model, resulting in a smooth curve and low SSE. For case 2 test 2, the overshoot is reduced to $\approx$ 20 bar while the frequency of the fast oscillations is 2.5Hz.

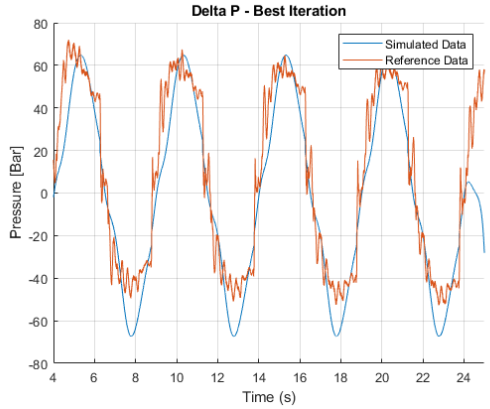

(a) Case 3 test 1

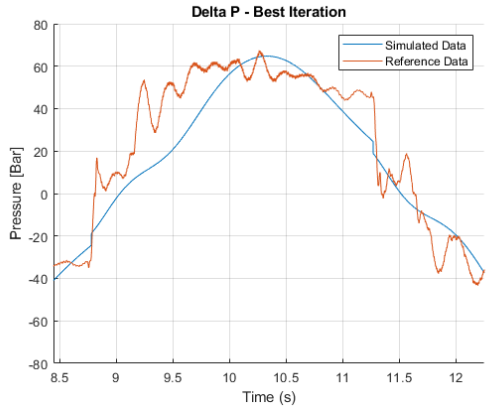

(b) case 3 test 1 zoomed view

Figure 3.4

$k0\_y$	$k1\_y$	$b0\_y$	$b1\_y$
7000	1000	350	10

Table 3.4. Optimal values of $k0\_y$, $k1\_y$, $b0\_y$, and $b1\_y$ for case 3 test 1

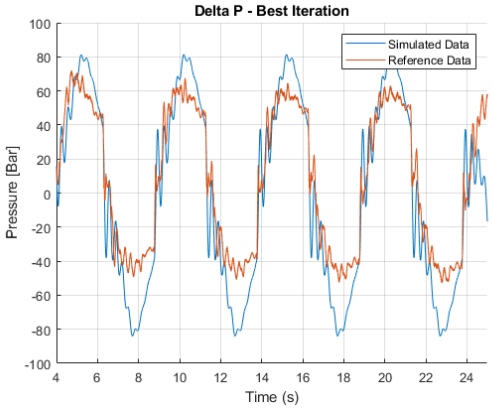

(a) Case 2 test 2

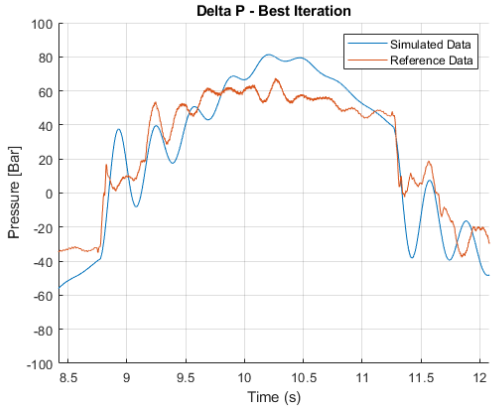

(b) case 2 test 2 zoomed view

Figure 3.5

$k0\_y$	$k1\_y$	$b0\_y$	$b1\_y$
45000	500	400	10

Table 3.5. Optimal values of $k0\_y$, $k1\_y$, $b0\_y$, and $b1\_y$ for case 2 test 2

The optimal parameters are determined to be case 2 test 2 as the high frequent oscillations can not be disregarded, even though case 3 test 1 produced lower SSE values.

It should be noted that the test data from the reference case shows an uneven behavior when turning left and right; the left chamber pressure consequently reaches a higher pressure in the peaks, which creates an uneven ΔP. This is why the reference data varies between -40 to $+60$. The data can be found in appendix F.

3.1 Simulation Results

In this section, the model is compared with other references from the data provided by Danfoss. The test that will be used for comparison are with:

- Higher tire pressure
- Concrete surface
- 10 tons load in the bucket

Due to the instance where ΔP is not symmetric at right and left turns, the absolute value of SSE can not be used to compare the different scenarios. The test results will be evaluated based on their ability to follow a similar oscillation pattern, together with the general amplitude of the pressure difference.
First, the tests are compared without modifying the model, and then the parameters are estimated to find a correlation.

Higher tire pressure

The increase in tire pressure increases both the damping and spring stiffness in the tire, resulting in faster vibrations in the vehicle. The result of increasing the tire pressure to 5 bar without tuning the model is shown in figures 3.6a and 3.6b, it is observed the vehicle dynamics fits well, matching the general amplitude of the reference data. For the faster oscillations, the frequency is lower, and the amplitude is higher when compared to the reference case. The tuned model response is shown in figures 3.7a and 3.7b, where the main difference is an increase in the fast oscillation frequency to $\approx 3.5Hz$. The difference in SSE is negligible.

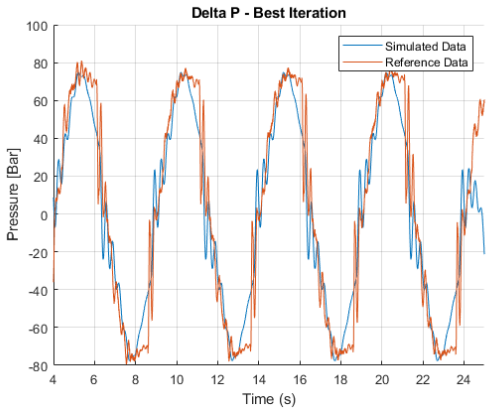

(a) 5 bar test with regular model parameters

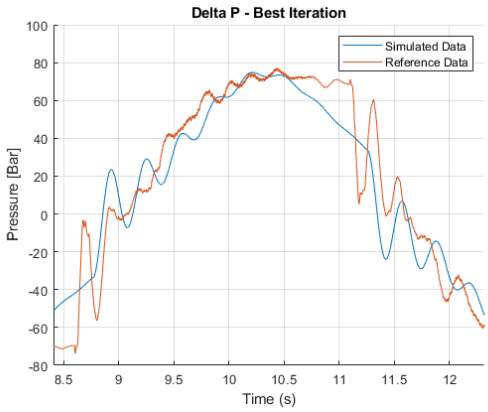

(b) Zoomed view of the 5 bar test with regular model parameters

Figure 3.6

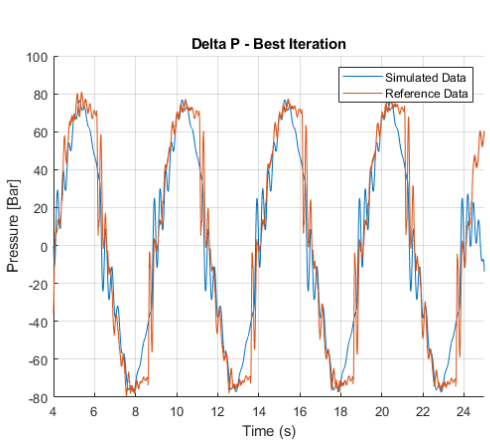

(a) 5 bar test with tuned model parameters

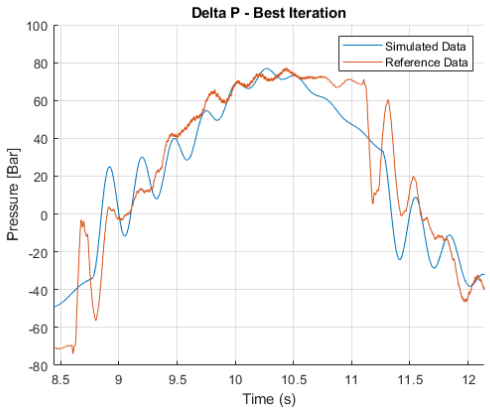

(b) Zoomed view of the 5 bar test with tuned model parameters

Figure 3.7

Concrete surface

In this test, the driving surface has changed from gravel to concrete. Concrete is harder and smoother than gravel; the general surface is more even, but any obstacles on the surface affect the vehicle more due to the hard structure. The result of a smoother driving surface can be seen in the test data where the pressure difference is ±40 bar whereas in the 5 Bar case, it is ±80 Bar. In this case, the bucket arm has been moved closer to the vehicle body, which lowers the moment of inertia. Moving the bucket arm closer also changes the friction distribution on the tires backward due to the rear tires experiencing more load. Increasing friction on the rear tires linearly affects the cylinder moment, as shown in figure 3.8. Since the bucket in this test is empty and the movement is minor, the friction is assumed to be similar to that in the initial case.

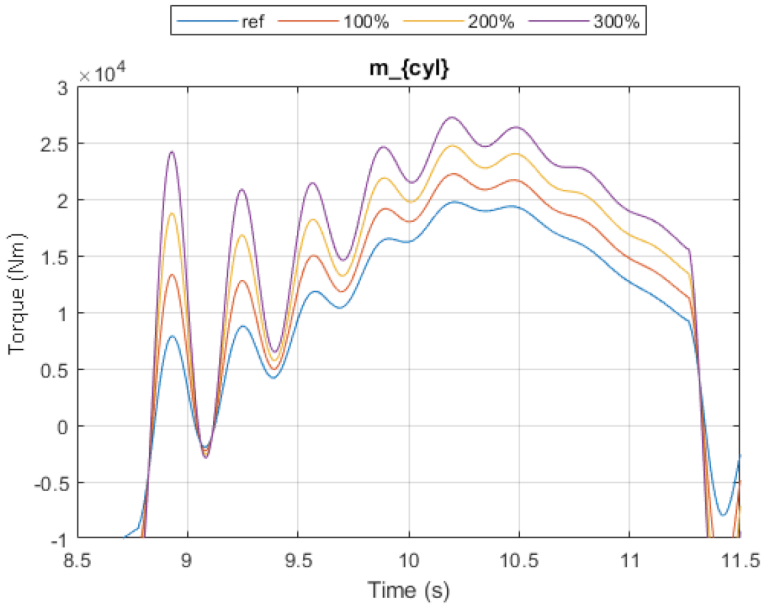

Figure 3.8. Rear friction affect on cylinder moment.

With the adjusted inertia the model was not able to predict the pressure difference, from

figures 3.9a and 3.9b it can be seen how the simulated ΔP overshoots the measured data by $\approx 50\%$. The model showed similar poor performance with the estimated parameters (figures 3.10a and 3.10b), indicating an issue in calculating the vehicle dynamics.

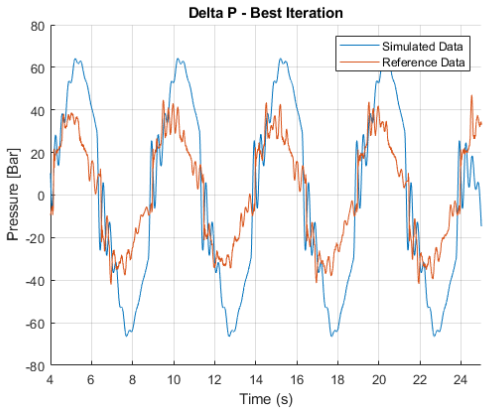

(a) Concrete test with regular model parameters

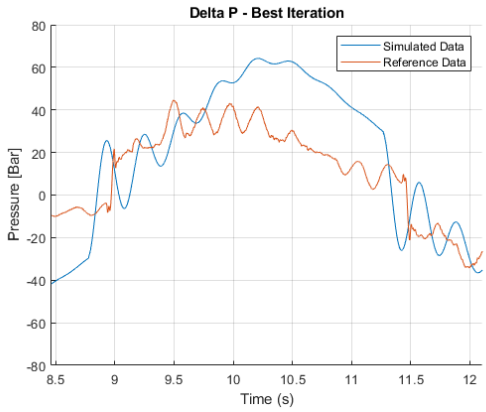

(b) Zoomed view of the concrete test with regular model parameters

Figure 3.9

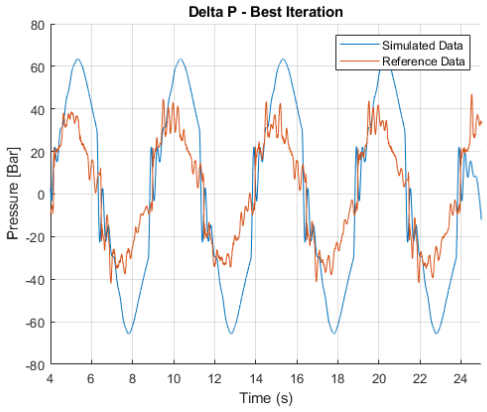

(a) Concrete test with tuned model parameters

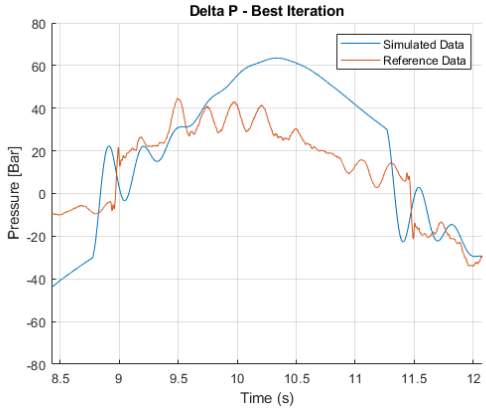

(b) Zoomed view of the concrete test with tuned model parameters

Figure 3.10

10 tons bucket load

In this test, the bucket position is placed at the initial position, and the bucket is loaded with 10 tons. The updated inertia is calculated by equation (3.2) assuming that the force is a point mass in the middle of the bucket

$$J_{10ton} = J_{terex} + m_{bucket} \cdot r^2 \tag{3.2}$$

where m_{bucket} is the mass added to the bucket and r is the distance from the original center of mass to the point mass. This moves the center of mass forward, which increases the friction on the front tires. From figures 3.11a and 3.11b is it observed that similar to the concrete case, the model is not able to predict ΔP accurately when varying the inertia.

The model did not show significant improvement with estimated parameters as shown on figures 3.12a and 3.12b.

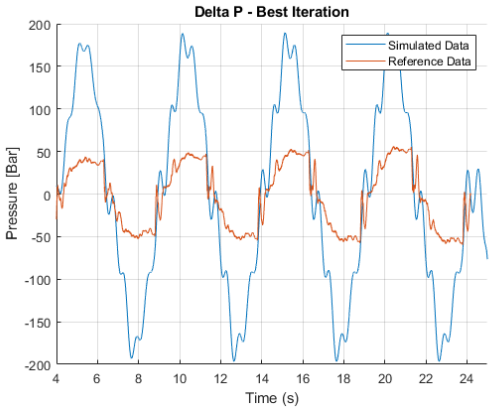

(a) 10 tons bucket load test with regular model parameters

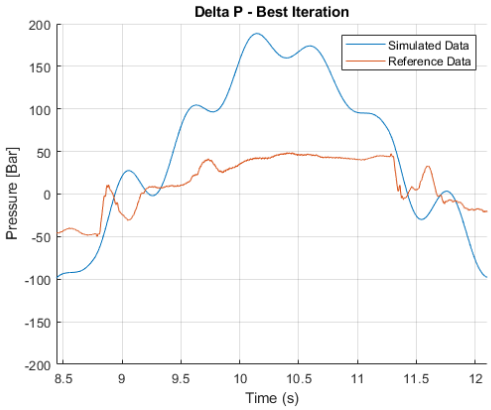

(b) Zoomed view of the 10 tons bucket load test with regular model parameters

Figure 3.11

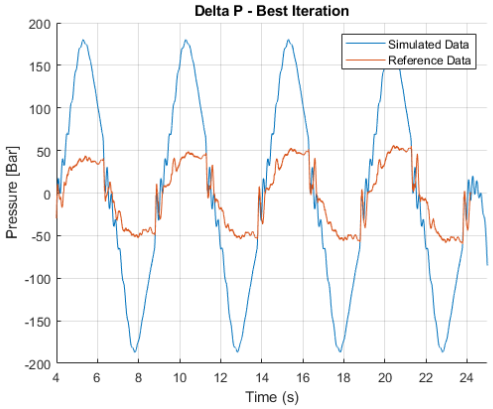

(a) 10 tons bucket load test with tuned model parameters

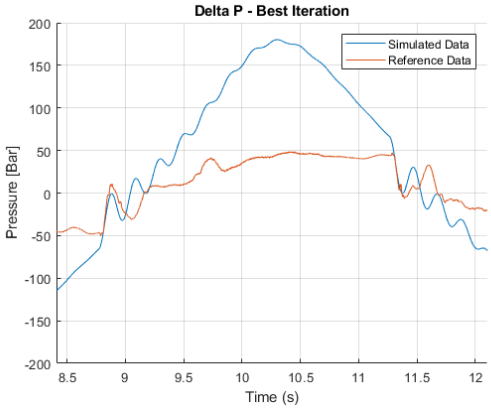

(b) Zoomed view of the 10 tons bucket load test with tuned model parameters

Figure 3.12

Since the model lacks the ability to estimate ΔP accurately in this state, no more experiments will be performed.

Inertia influence The high impact of increasing inertia is investigated as this significantly affects the model accuracy. From the moment balance in equation (2.9), M_{cyl} consists of three components, M_{fric}, M_{tire}, and $J \cdot \ddot{\alpha}$. The magnitude of the components in the reference case is shown in figure 3.13a, here it is shown how the friction in the hydraulic cylinders is negligible, while the tire torque and inertia component have significant impact. With a load of 10 tons in the bucket the result can be seen in figure 3.13b, the contribution from the inertia increases by $\approx 150\%$. This dilutes the contribution from M_{tire}, which has little to no influence. Furthermore, the total value of the cylinder moment increases such that ΔP increases out of range considering the measured data from the previous scenarios.

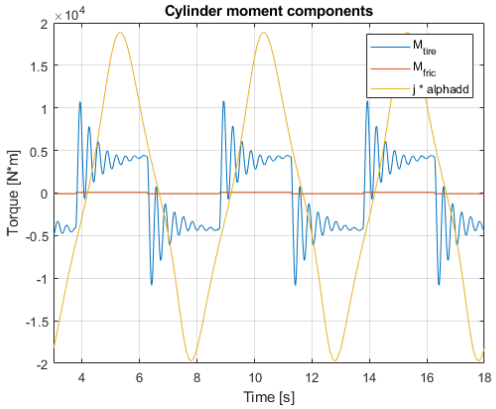

(a) Comparison of cylinder moments components - reference case

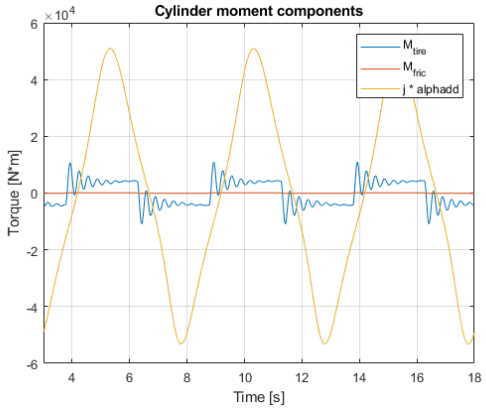

(b) Comparison of cylinder moments components - 10 tons bucket load case

Figure 3.13

Discussion 4

The procedure used in this project was to combine the unknown parameters into a simple mass spring damper system for each tire. The difficulty in describing the pressure difference when varying the inertia suggests some underlying dynamics that are not included in the dynamic model.
The results show that the model is sensitive to changing inertia. This may be due to some of the assumptions made during model development. The vehicle is assumed to have a total mass with the center of mass located directly above the pivot point. When the vehicle turns, the center of mass moves along with the pivot point, whereas in reality, the vehicle has two masses that shift less sideways but also move a bit forward and backward.
The current model assumes that all four tires have identical spring, damping, and friction parameters, which simplifies the computation but limits accuracy. In reality, each tire experiences different loads and conditions, especially during maneuvers. Modeling these differences would require a significant increase in computational effort but is crucial for accurately simulating the vehicle's behavior. This approach would involve defining individual parameters for each tire, taking into account their unique interactions with the road and load conditions.
The model considers only the lateral motion, meaning that the speed in the longitudinal direction is disregarded together with longitudinal slip, air resistance, ground unevenness, and camber angle. The ground unevenness is difficult to model as this depends on various unpredictable factors. The model did show the ability to move from gravel to concrete with acceptable accuracy. The combination of these forces may have a some impact on the vehicle.
The validation data provided by Danfoss showed uncertainties in some cases where the pressure difference is not even when turning right or left. This makes the SSE dilutes when analyzing the parameter estimation and comparing the cases. The parameters were estimated to generally have low values for the variable terms and high values for the constant terms; this yields a smooth curve that fits the general sine wave of the test data but small high-frequency oscillations. This eliminates the prediction of vibrations in the hydraulic cylinders, which is undesireable. Therefore, manual estimation was done to keep the desired pattern on ΔP.

Conclusion 5

This chapter will summarise the work done in the project and conclude on the project statement.

Is it possible to develop a lumped nonlinear dynamic tire model that can predict the influence of the tire on the Terex L310 steering system?

A simple approach to building a nonlinear dynamic tire model was chosen to reduce the complexity. The kinematics of the steering geometry was derived in Section 2.1, and the dynamic model was developed in section 2.2. The tire proved to be a complex structure with an extensive amount of unknown parameters that could not all be described by a single mass spring damper system. The system tested well on the reference case and was able to predict the pressure difference with reasonable accuracy when running a 0.2Hz snake test on gravel. The optimal set of parameters was found for the reference case to match the frequency and amplitude to the overall pressure difference and the high-frequency vibrations, improving the accuracy by 5%. The model was tested to fit other environments and workload situations using data provided by Danfoss. The model was able to match the frequency of the vibrations well when increasing the tire pressure to 5 Bar. In the test cases with different inertia, the model was not able to describe the pressure difference within a reasonable error. The change in inertia proved to dominate the overall amplitude of the cylinder force. The variable parameters were not able to compensate for this change, resulting in a large error in the simulations.
The mass spring damper model strategy, combined with the assumptions that the vehicle can be described with one body and all tires share the same parameters, proved unable to describe the impact of the tire on the steering system. Varying the parameters individually demands too large of a computational effort, and due to the lack of time, could not be tested properly.

Future Works 6

The current study lays the groundwork for understanding and modeling tire dynamics in articulated frame-steered vehicles. However, there are several areas where the research can be expanded to enhance the model's accuracy and applicability.

Speed and Longitudinal Slip Future models should integrate longitudinal dynamics, such as vehicle speed and longitudinal slip. Longitudinal slip is important for understanding tire-road interaction during acceleration and braking. Including these dynamics will help in capturing the complete behavior of the vehicle. When reaching higher speeds, the aerodynamics around the tire can start to affect the behavior, incorporating a drag coefficient based on the aerodynamics can increase the simulation accuracy.

Error comparison The comparison of results using SSE yielded some undesirable outcomes relative to the desired results. This issue can be mitigated by creating segmented areas for SSE, allowing for separate comparisons in the high-frequency and low-frequency ranges, or by using a different method altogether.

Individual Parameters Extended Modeling to account for individual spring, damper, and friction parameters for each tire, the model should be expanded from a lumped parameter model to a more detailed multibody dynamics model. This requires defining the unique characteristics of each tire based on its position, load, and interaction with the road.

Advanced material modelling The tire's material properties play a crucial role in its dynamic behavior. Future work could involve advanced material modeling techniques to better capture the viscoelastic properties of the tire rubber.

Machine learning Machine learning offers the ability to train a neural network to predict the tire forces, an alternative approach to the problem. This requires large amounts of data and computational effort, though only while training the system.

Bibliography

[1] E. N. Olesen, "Active damping of a hydrostatic steering circuit, for an articulated vehicle," 2020.

[2] C. Equipment, *Articulated vs rigid haulers - choose the right truck*, `https://www.cjd.com.au/about/news-events/industry-news/mining/articulated-vs-rigid-haulers/`, [Accessed 21-02-2024].

[3] G. Genta, "Conventional and slip steering for multi-wheel planetary rovers," 2016.

[4] R. N. Jazar, *Vehicle Dynamics*. 2008.

[5] L. L. Egbert Bakker Hans B. Pacejka, "A new tire model with an application in vehicle dynamics studies," *SAE Transactions*, 1989.

[6] M. G. Bakker, "Ftire, a new fast tire model for ride comfort simulations," *Esslingen University of Applied Sciences*, 1999.

[7] e. a. Thomas H. Langer Thorkil K. Iversen, "A ride comfort tyre model for off-highway vehicles," *International Journal of Vehicle Design*, 2014.

[8] e. a. Nan Xu Hassan Askari Yajjun Huang, "Tire force estimation in intelligent tires using machine learning," 2020.

Wheel Load Data Sheet A

Figure A.1. Wheel loader datasheet page 1

TECHNICAL SPECIFICATION L310

Technical specifications

ENGINE

Net power rating at 2200 rpm (ISO 9249).....149 kW / 2200 min^{-1}	Number of cylinders.....6	Battery.....2 x 12 V / 100 Ah / 900 A
Make / model ..... Cummins QSB 6,7 T4Final	Cooling system.....Water-cooled	Alternator..... 24 V / 70 A
Design.....Turbocharger / charge-air cooling	Air filter..... Cyclone air filter	Starter..... 24 V / 4,8 kW
Torque..... 929 Nm / 1500 min^{-1}		

HYDRAULIC SYSTEM

• Max. flow..... 220 l/min	• Load-sensing pump variable displacement pump for working hydraulic	• 3rd Hydraulic loop as standard
• Max. operating pressure ..... 350 bar	• Hydraulic oil cooling with thermostat	• Pilot operated control circles for Lift/Lower, Dump, Tilt
• Return - Suction oil filter	• Proportional and sensitive operation with LUDV control block	• All main functions control trough one joystick

LOADING EQUIPMENT

• Combined P+Z Kinematic	• Lifting.....6,5 s	• Standard bucket for general purpose 3,1 m^3 with material density 1,8 kg/dm^3
• 2x Lifting cylinders	• Lowering.....4 s	• Lift capacity at ground level (ISO 14397-2)..... 232 kN*
• 1x Bucket cylinder	• Dumping .....2,8 s	• Breakout force at bucket edge (ISO 14397-2) with quick-attachment...129 kN*
• Parallel lifting due to combined kinematic	• Tipping.....2,5 s	• Breakout force at bucket edge (ISO 14397-2) with direct mounted..... 154 kN*
	• Total cycle time .....15,8 s	** with standard bucket*

DRIVELINE

• Continues variable transmission	• Traveling using inch pedal	• Multi-disc brakes on both axels, with separate circles
• Suction - Return filter	• Two variable displacement motors driven by one variable displacement pump	• Slow drive.....0 - 6 km/h
• Automotive drive	• Tractive effort .....135 kN	• Fast drive.....0 - 40 km/h
• Close loop system	• Parking brake on rear axle	

STEERING

• 2 x Steering cylinders	• Proportional hydraulic steering	• Quick steering with only 45° steering wheel turn
• Load-sensing variable displacement pump	• Electrical emergency pump as standard	• 80° total steering angle

AXLES

• Front rigid axle	• 30% self differential lock	• Planetary gear set in wheel hub
• Read oscillation axle	• Oscillation angle.....± 12°	• Flange mass.....2180 mm

CAB

• ROPS tested ISO 3471	• 2 x doors with 180 aparture angle	• Cushion adjustable driver seat
• FOPS tested ISO 2449	• 2 x front and read lights on the roof	**SOUND LEVELS:**
• A/C and heating unit	• Electrical front and read windshield wipers	• ISO 6396 (L_pA) in driver's cab.....79 dB (A)
• Ergonomical design	• Combi-instrument with CAN network	• 2000/14 EG (L_wA) ambience level.....104 dB (A)

FILL CAPACITIES

• Fuel tank .....250 l	• AdBlue© .....34 l	• Axles middle hub, each axle.....20 l
• Cooling system.....38 l	• Hydraulic oil total .....165 l	• Axle wheel hub, each axle.....5 l
• A/C.....900 g	• Hydraulic oil tank .....134 l	• Gear box .....4,3 l
• Engine oil.....15 l		

2 WHEEL LOADER L310

Figure A.2. Wheel loader datasheet page 2

WORKING EQUIPMENT L310

TIRES

• 23.5R25 EM60 16PR Mitas.....Standard	• 23.5R25 RL-5K Goodyear	• 750/65R25 TL-3A+ Goodyear
OPTION:	• 23,5R25 RT-3B Goodyear	• 750/65R25 VTS Brudgestone
• 23.5R25 VJT L3 Bridgestone	• 23,5R25 XHA 2 Michelin	• More available on request

ADDITIONAL STANDARD EQUIPMENT

• Air Conditioner	• Operating data display screen	• Proportional joystick for 3rd hydraulic circle
• Prepared for Radio	• SCR and DOC Catalysators	• Main battery switch operating in cab
• Steering column height and tilt adjustible	• Reversible Fan	

OPTIONAL EQUIPMENT

• Quick attachment	• Camera	• Guard for front and read lights
• 4rd hydraulic circle	• Bacon light	• Backalarm for reverse traveling
• Refuling pump	• Gear protection	• Automatic bucket positioning
• Central lubrication	• Anti- Tief device	• Trailer coupling
• Radio	• Pressurised cabin	• Speed limitation
• LED working lights	• TÜV	• Corrosion protect against salty environment
• Fog lights. 2x front or 2x frond and 2 in middle of machine	• Ride control	• And more available on request

FORK LIFT ATTACHMENT

• Operating load over the total lift and steering range.....9000 kg	• Length pallet forks (150 x 70 mm)....1200 mm	• Operating load determined on level ground = 80% of tipping load, articulated
• Width of fork carrier.....1900 mm	• Stability factor.....1,25	

BUCKET TYPE*

	QA D	Volume	Material density	Teeth Cutting edge	Fill factor	Dumping height (A)
General-purpose bucket, round form	QA	3,0 m^3	1,8 kg/dm^3	Teeth	100%	N/A
General-purpose bucket	D	3,1 m^3	1,8 kg/dm^3	Teeth	105%	N/A
General-purpose bucket	QA	3,0 m^3	1,8 kg/dm^3	Teeth	100%	N/A
General-purpose bucket, round form	D	3,1 m^3	1,8 kg/dm^3	Teeth	105%	N/A
General-purpose bucket, round form	QA	3,0 m^3	1,8 kg/dm^3	Cutting edge	100%	N/A
General-purpose bucket, round form	D	3,1 m^3	1,8 kg/dm^3	Cutting edge	105%	N/A
Earth bucket	QA	3,2 m^3	1,6 kg/dm^3	Teeth	110%	N/A
Light-material bucket	D	4,0 m^3	1,2 kg/dm^3	Cutting edge	110%	N/A
Light-material bucket	D	5,0 m^3	0,8 kg/dm^3	Cutting edge	110%	N/A
Light-material bucket	QA	4,8 m^3	0,8 kg/dm^3	Cutting edge	110%	N/A
Light-material bucket	D	6,5 m^3	0,6 kg/dm^3	Cutting edge	110%	N/A
High-tip bucket	D	4,5 m^3	0,8 kg/dm^3	Cutting edge	110%	N/A
High-tip bucket	D	6,0 m^3	0,6 kg/dm^3	Cutting edge	110%	N/A
High-tip bucket	QA	4,3 m^3	0,8 kg/dm^3	Cutting edge	110%	N/A
HD bucket	D	3,0 m^3	1,8 kg/dm^3	Teeth	105%	N/A

*general safety factor by ISO 14397–1, S=2

ATLAS 3

Figure A.3. Wheel loader datasheet page 3

DIMENSIONS L310

Dimensions with standard Bucket

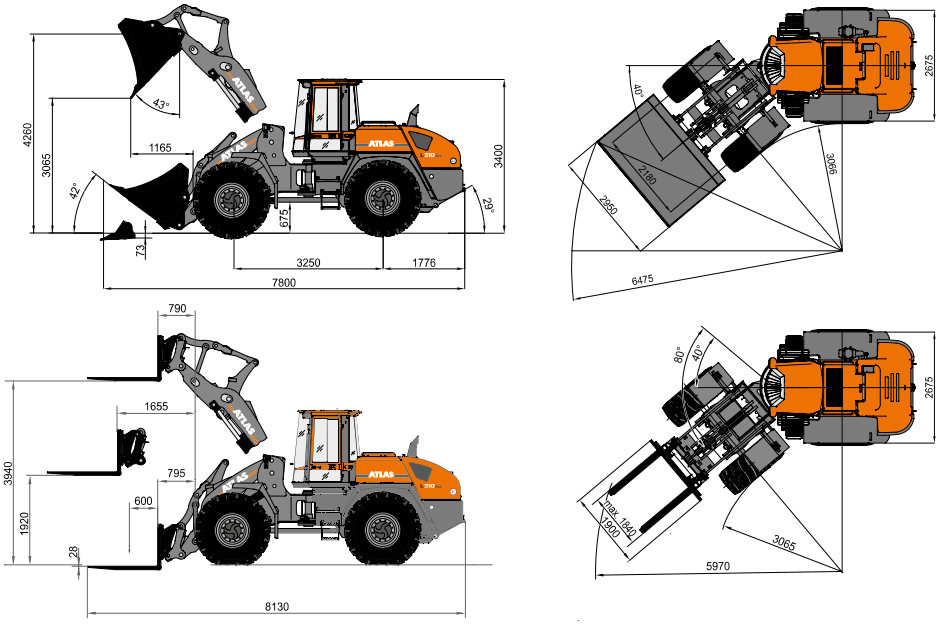

EXAMPLES OF MATERIAL DENSITY (t/m³)

Construction	sediment 2.1	paper 0.9
concrete 1.9	crushed stone 1.5	slag 1.0
soil (dry) 1.5	de-icing salt 1.3	slag concrete 2.7
soil (watery) 2.0	clay 1.6	**Landscaping, Agriculture**
rock (fill) 2.4	cement 1.7	agricultural crop 0.7
granite 1.8	clinker (stacked) 1.8	grain 0.6
limestone 1.6	**Industry**	hay 0.3
gravel (dry) 1.9	ember 0.7	potash 1.1
gravel (watery) 2.1	brown coal briquette 0.8	compost 1.0
loam 1.7	ferrous product 7.8	flour 0.5
plaster 2.2	iron ore 2.3	clay (watery) 2.3
sand (dry) 1.9	cullet 1.9	phosphate fertiliser 2.2
sand (watery) 2.1	gas coke 0.4	turf (watery) 1.1
sandstone 2.4	timber 0.8	turf (dry) 0.4
shale 2.2	mineral coal 1.2	mineral fertilizer 1.0

www.atlasgmbh.com
ATLAS GmbH
Atlasstrasse 6, 27777 Ganderkesee, Germany
T: +49 (0) 4222 954 0, F: +49 (0) 4222 954 343
info@atlasgmbh.com

Figure A.4. Wheel loader datasheet page 4

Bias Tire B

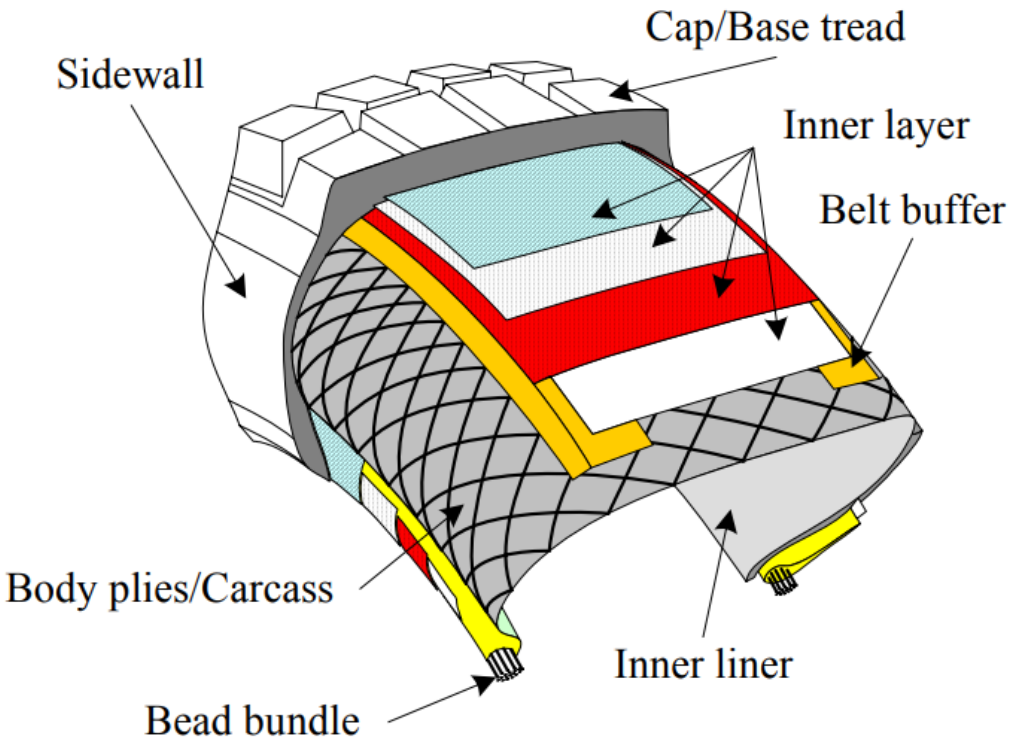

Figure B.1. Examples of a non-radial tire's interior components and arrangement.[4]

Sensitivity analysis C

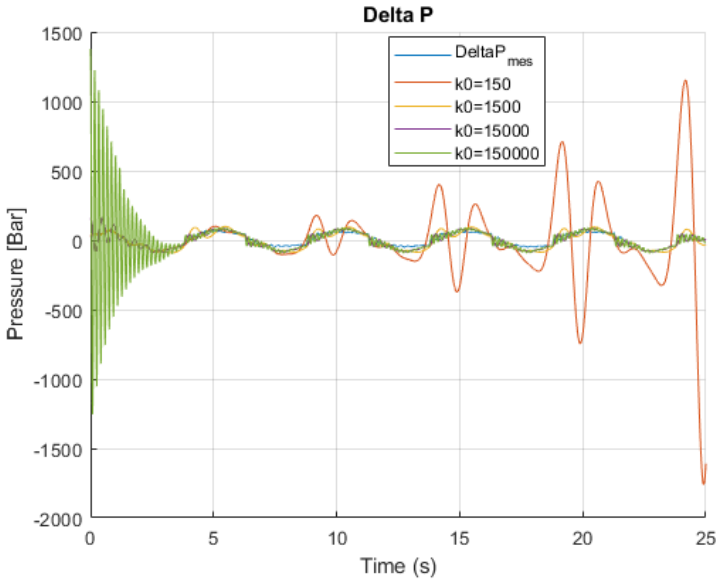

Figure C.1. Affect of k0 on ΔP

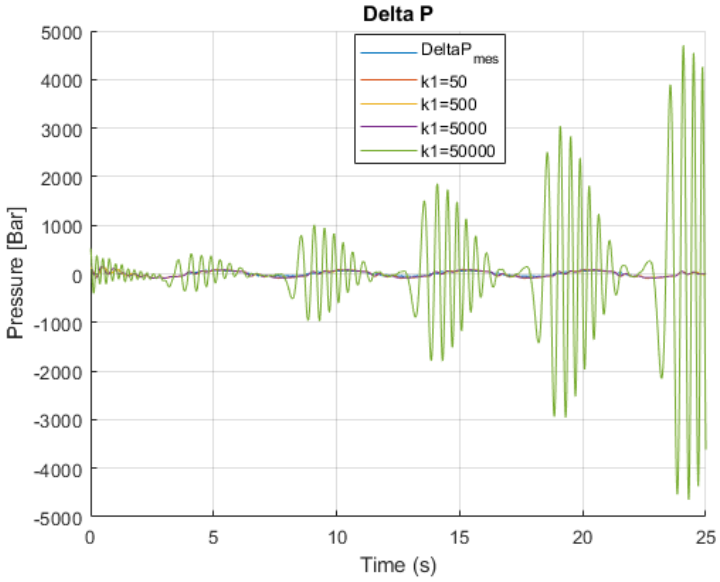

Figure C.2. Affect of k1 on ΔP

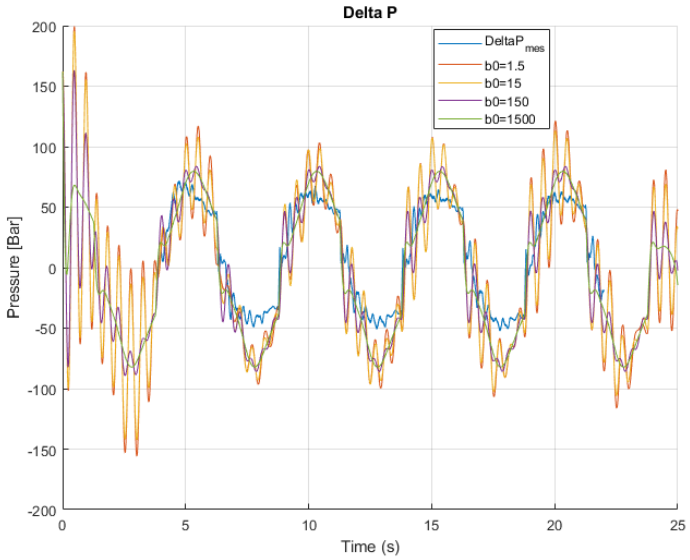

Figure C.3. Affect of b0 on ΔP

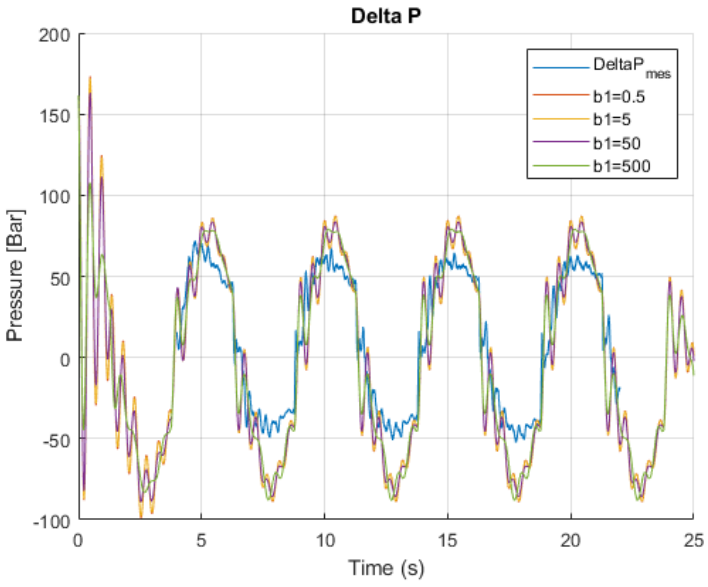

Figure C.4. Affect of b1 on ΔP

Parameter estimation D

Test 1	k0	k1	b0	b1
Initial value	7000	1000	50	10
Increment	10000	5000	100	50

Test 2	k0	k1	b0	b1
Initial value	15000	500	100	10
Increment	10000	1000	100	10

Test 3	k0	k1	b0	b1
Initial value	5000	10000	10	100
Increment	1000	10000	10	100

Case 1	$\mu_{v,terex}$	$\mu_{c,terex}$	$\mu_{v,tire}$	$\mu_{c,tire}$
Initial value	0.003	0.005	0.05	0.07

Case 2	$\mu_{v,terex}$	$\mu_{c,terex}$	$\mu_{v,tire}$	$\mu_{c,tire}$
Initial value	0.003	0.0005	0.2	0.5

Case 3	$\mu_{v,terex}$	$\mu_{c,terex}$	$\mu_{v,tire}$	$\mu_{c,tire}$
Initial value	0.003	0.005	0.2	0.1

Case 4	$\mu_{v,terex}$	$\mu_{c,terex}$	$\mu_{v,tire}$	$\mu_{c,tire}$
Initial value	0.003	0.005	0.05	0.03

Case 5	$\mu_{v,terex}$	$\mu_{c,terex}$	$\mu_{v,tire}$	$\mu_{c,tire}$
Initial value	0.003	0.005	0.05	0.07

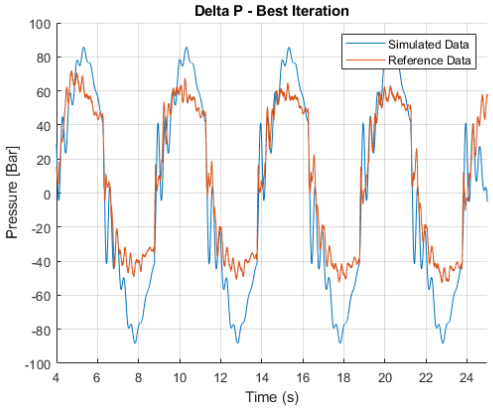

(a) Results of case 1 test 1

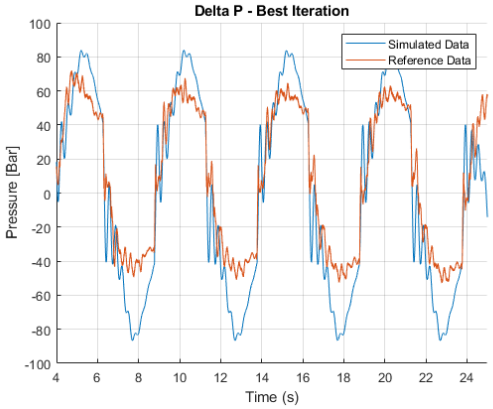

(b) Results of case 1 test 2

Figure D.1

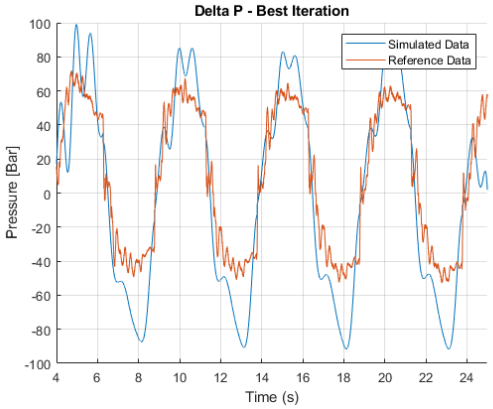

(a) Results of case 1 test 3

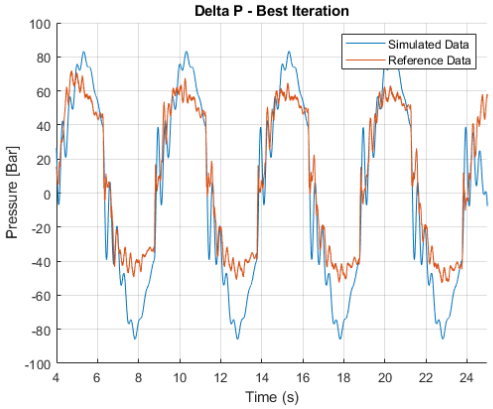

(b) Results of case 2 test 1

Figure D.2

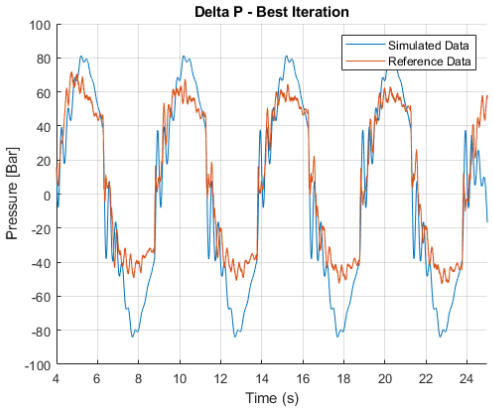

(a) Results of case 2 test 2

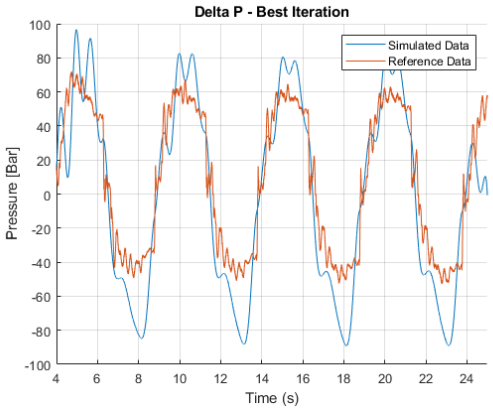

(b) Results of case 2 test 3

Figure D.3

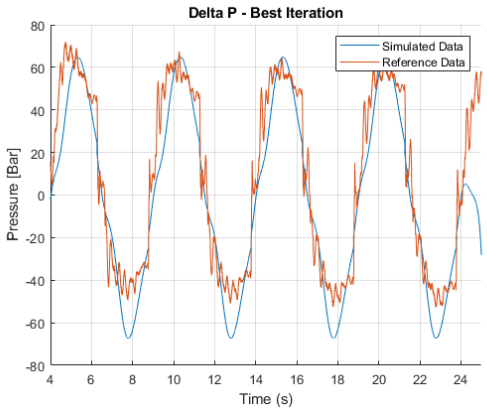

(a) Results of case 3 test 1

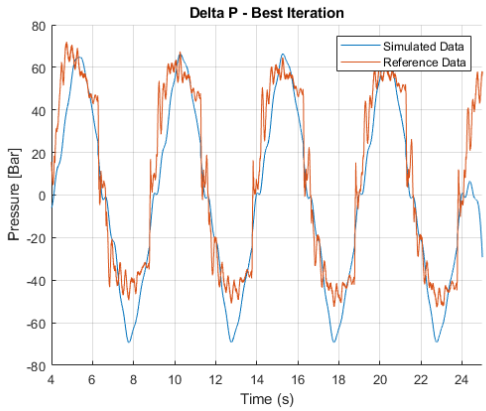

(b) Results of case 3 test 2

Figure D.4

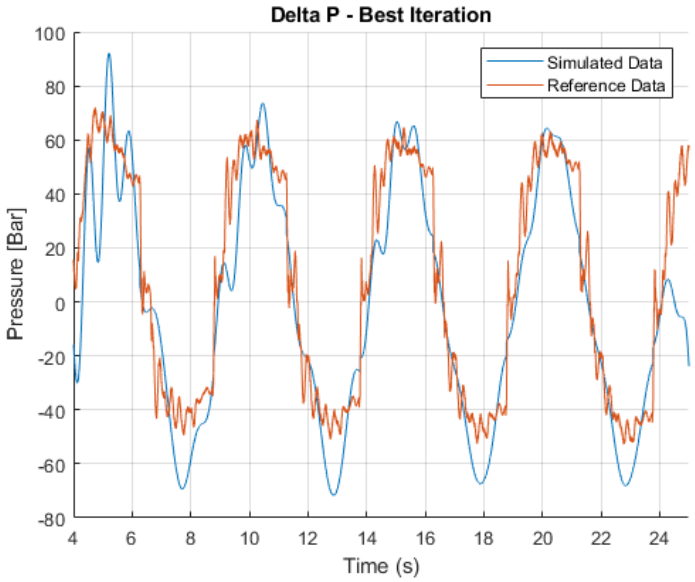

Figure D.5. Results of case 3 test 3

23.5R25 BRIDGESTONE VJT E

23.5R25 BRIDGESTONE VJT DE2 * 195A2 TL DEMOUNT

BRIDGESTONE

This 23.5R25 Bridgestone OTR tyre will meet your needs! This tyre is perfectly suited for loaders. This OTR tyre also has a pattern depth of 35 mm. It should preferably be used with a pressure of 6.5 bar. The 23.5R25 Bridgestone should ideally be mounted on a 19.50 rim.

Information

Article number	B23500025BRVJT05
Brand	Bridgestone
Profile	VJT
TRA	L-3
L/S	195A2
Star rating	★
TL/TT	TL
Application	
Radial/diagonal	Radial
Recommended rim	19.50
Air pressure (bar)	6.5
Include inner tube	No
Condition	Demo

Sizes & weights

Size	23.5R25
Width (mm)	616
Diameter (mm)	1,602
Loaded radius (mm)	696
Rolling circumference (mm)	695
Tread (mm)	35
Weight	331 Kg
Load capacity kg at km/h (1)	12150 - 10

Figure E.1. Datasheet for Bridgestone 23.5R25 VJT tire

Reference data F

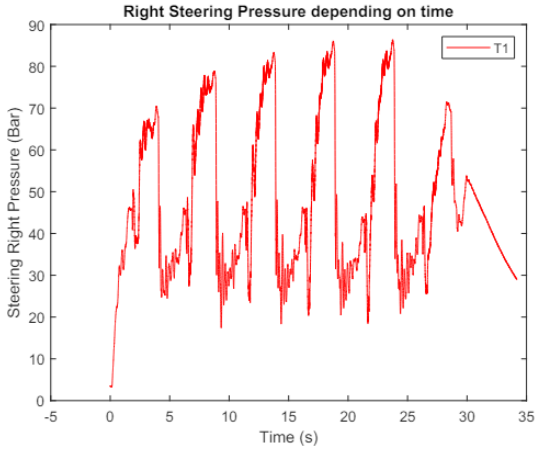

(a) Reference case right side

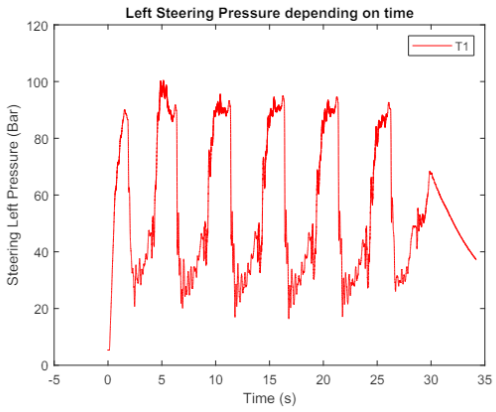

(b) Reference case left side

Figure F.1